Opposing spatial gradients of inhibition and neural activity in mouse olfactory cortex

Adam M. Large, Nathan W. Vogler, Martha Canto-Bustos, Paul Schick and Anne-Marie M. Oswald

Department of Neuroscience, Center for the Neural Basis of Cognition,

University of Pittsburgh, Pittsburgh, PA, United States, 15213

Corresponding Author:
Anne-Marie M. Oswald
Assistant Professor
Department of Neuroscience
University of Pittsburgh
A210 Langley Hall
Pittsburgh, PA, 15260
amoswald@pitt.edu

Abstract

The spatial representation of stimuli in primary sensory cortices is a convenient scaffold for elucidating the circuit mechanisms underlying sensory processing. In contrast, the anterior piriform cortex (APC) lacks topology for odor identity and appears homogenous in terms of afferent and intracortical excitatory circuitry. Here, we show that an increasing rostral-caudal (RC) gradient of inhibition onto pyramidal cells is commensurate with a decrease in active neurons along the RC axis following exploration of a novel odor environment. This inhibitory gradient is supported by somatostatin interneurons that provide an opposing, rostrally-biased, gradient of inhibition to interneurons. Optogenetic or chemogenetic modulation of somatostatin cells neutralizes the inhibitory gradient onto pyramidal cells. This suggests a novel circuit mechanism whereby opposing spatial gradients of inhibition and disinhibition regulate neural activity along the RC-axis. These findings challenge our current understanding of the spatial profiles of neural circuits and odor processing within APC.

It is well established that the spatial organization of sensory information plays an important role in neocortical sensory processing. The retinotopic, tonotopic and somatotopic maps established at the periphery form the basis of stimulus representation in primary visual, auditory and somatosensory cortices. This spatial organization is perhaps the oldest and best understood feature of sensory codes.

In the olfactory system, odor components are encoded by individual olfactory receptor neurons (ORNs) that express a single receptor gene. All ORNs expressing the same receptor project axons to ~2 target glomeruli in the olfactory bulb (OB) [1,2]. Within the OB, individual mitral/tufted (M/T) cells extend apical dendrites to a single glomerulus [3] and respond selectively to glomerular activation [4,5]. This extreme connection specificity produces a discrete spatial organization of odor information within the OB [6-9]. However, just one synapse away in the anterior piriform cortex (APC), any semblance of spatial representation for odor identity is lost.

The piriform cortex is a trilaminar cortex that extends along the rostral-caudal (RC) axis of the ventral rodent brain. The two main subdivisions, anterior (APC) and posterior (PPC) piriform cortex, differ with respect to afferent and efferent projections [10-12] as well as functional roles in olfactory processing [13-16]. However, despite the fact that each region comprises ~1-2 mm of the RC axis, odor processing within APC or PPC is considered spatially homogenous. The APC is delineated by the lateral olfactory tract (LOT) that delivers odor information directly from the OB. Single M/T cell axons branch extensively along the LOT [17-19] resulting in diffuse pattern of afferent excitation. Likewise, recurrent connections between principal neurons within APC extend over millimeter distances [20,21]. Consistent with this distributed excitatory architecture, there is no topography for odor identity in APC. Neurons responsive to a single odor are distributed along the RC-axis of the APC [22-24] and nearby neurons respond to different odors [24-27]. The absence of an “odortopic” map, suggests that, unlike sensory neocortex, space is not a dimension for odor coding in APC.

Nonetheless, there is evidence that odor evoked responses vary along the rostral-caudal axis of APC. For example, odor evoked activity at rostral sites is denser [22], has lower concentration thresholds [28], and has earlier response times [24,29-31] versus caudal sites. Further, in contrast to excitation, intracortical inhibition is asymmetric along the RC axis [32]. Finally, rostral APC projects more densely to

the OB and orbitofrontal cortex (OFC) while caudal APC and PPC project to agranular insula (AI) [11,33-35]. Thus, contrary to preconceived notions, space may be a relevant feature of olfactory processing in APC. However, a central challenge is elucidating the circuit mechanisms and functional roles of RC spatial patterning in APC.

In this study, we use optogenetic [36] and chemogenetic tools [37] as well as targeted-recombination in active populations (TRAP) [38] to investigate the circuitry underlying the spatial profiles of inhibition and neural activity in APC. Specifically, we find that inhibition of pyramidal cells (PC) increases on a millimeter scale from rostral to caudal APC. Our findings suggest a disinhibitory circuit mechanism, mediated by somatostatin interneurons, underlies the RC patterning of inhibition. This increasing gradient of inhibition is commensurate with a context dependent, RC decrease in the density of active neurons during odor exposure. Moreover we show that spatial patterning of inhibition and neural activity is laminar dependent. Altogether, our findings provide new insights to the RC spatial patterns of inhibition and neural activity in APC and suggest space is a dimension of olfactory processing in cortex.

Results

Asymmetric inhibitory circuitry in APC

Spatially asymmetric inhibition of pyramidal cells (PC) in APC [32] has been previously demonstrated using glutamate uncaging. Specifically, light evoked uncaging at caudal stimulation sites yielded stronger inhibition of PCs compared to rostral sites. These findings are seemingly at odds with the spatial profiles of excitation [17-21] and odor-evoked responses [26,27] that do not vary with space. This led us to question, “How and why do inhibitory spatial asymmetries exist in APC?”

Since previous un-caging methods could activate both excitatory and inhibitory neurons, we investigated whether inhibitory circuits alone are sufficient to reproduce inhibitory asymmetries. Whole cell recordings were made from L2 principal excitatory neurons, namely semilunar cells (SL) and superficial PCs (sPC) as well as deep PCs (dPC) in L3. Recorded neurons were centrally located along the RC axis in sagittal slices of APC. Interneurons were specifically activated using Channelrhodopsin

92 (ChR2) expressed under the promoter for vesicular GABA transporter (VGAT). VGAT-ChR2
93 interneurons were stimulated using restricted spots (~70 μm diameter) of blue light in 4x5 grid
94 surrounding the recorded cell (schematic, **Figure 1A, D1** [39]). The inhibitory strength was quantified as
95 the area (pAs) under IPSC evoked at each stimulation site **(Figure 1B1,C1, D2)**. We have previously
96 reported the inhibitory strength by cell type and layer [39]. Here, we quantify the asymmetry in inhibitory
97 strength evoked at rostral versus caudal sites. An asymmetric bias index was calculated as the
98 difference in average inhibition at caudal versus rostral stimulation sites (I_C-I_R), divided by the sum of
99 the inhibition from both sides (I_C+I_R), (**Figure 1B2,C2,D3**). Thus, solely caudal inhibition produces a
100 bias value of +1 while -1 corresponds to rostral inhibition. Inhibition was not significantly asymmetric in
101 SL cells (bias: 0.08 ± 0.11, p: 0.49, n=13, **Figure 1B2**). However, sPCs (L2) and dPCs (L3) received
102 significant, caudally biased inhibition (sPC bias: 0.22 ± 0.08, p: 0.016, n=14, **Figure 1C2**; dPC bias:
103 0.19 ± 0.05; p: 0.0012, n=16, one sample t-test, **Figure 1D3**). Thus, inhibitory circuitry alone is
104 sufficient to reproduce asymmetric inhibition of PCs along the RC-axis. Since we have previously found
105 that inhibition of sPCs is significantly weaker than dPCs, and inhibition from L3 is stronger than L2 [39],
106 we focused the remainder of our experiments on L3 dPCs.

107 One interpretation of these findings is that caudally located dPCs receive stronger inhibition
108 than rostral dPCs. To investigate this possibility, we compared local inhibitory strength in dPC pairs
109 (n=19) separated by (100-1000 μm) distances along the ~1.5 mm RC-axis. On average, the caudal
110 neuron of the pair received significantly stronger inhibition (4.18 ± 0.90 pAs) than the rostral neuron
111 (2.60 ± 0.68 pAs, p: 0.002, paired t-test, **Figure 1E1**). Moreover, as the distance between the rostral
112 and caudal neuron increased, the difference in inhibitory strength increased (slope: 5.8 ± 2.1 pAs/mm,
113 p: 0.013, R^2: 0.32, **Figure 1E2**). Finally, across the population of dPCs, inhibitory strength increased
114 with soma location relative to the rostral start of the LOT in the sagittal slice (slope: 5.4 ± 1.3 pAs/mm,
115 p: 0.0003, n=27, R^2: 0.41, **Figure 1F**). These findings demonstrate an increasing gradient of inhibition
116 onto dPCs with a spatial scale that extends >1.0 mm of the RC axis of APC.

To test if stronger caudal inhibition is a general feature of APC we investigated inhibition of L2 and L3 interneurons using grid stimulation of VGAT-ChR2 interneurons (**Figure 2A**). L2 interneurons received weaker inhibition (3.42 ± 0.5 pA) than L3 interneurons (7.02 ± 0.92 pAs, p: 0.0043, ANOVA-Tukey, **Figure 2B**). In addition, L2 interneurons did not receive significantly asymmetric inhibition (bias: 0.04 ± 0.07, p: 0.11, n=18, **Figure 2C1, 2**). L3 interneurons received comparable inhibition to dPCs (8.63 ± 0.84, p: 0.239, ANOVA-Tukey, **Figure 2B**). However, L3 interneurons received stronger inhibition from rostral rather than caudal sites (bias: -0.13 ± 0.05, p: 0.013, n=25, **Figure 2D1,2**) and bias indices of L3 interneurons significantly differed from dPCs (p: 0.0001, t-test, **Figure 2E**). Thus, dPCs and L3 interneurons have opposing spatial profiles of inhibition- dPCs receive stronger inhibition from caudal sites versus rostral sites (I_C: 0.63 ± 0.034, I_R: 0.44 ± 0.042 p: 0.003, paired t-test) and L3 interneurons receive significantly more inhibition from rostral sites versus caudal (I_R: 0.54 ± 0.033, $I_{C:}$ 0.42 ± 0.034 p: 0.008, paired t-test **Figure 2F**).

How do inhibitory circuits implement opposing RC inhibitory asymmetries and what is the functional role of this opposition? A simple mechanism to increase inhibition is to increase the number of interneurons. Since the majority (~85%) of PC-targeting interneurons in L3 express parvalbumin (PV), somatostatin (SST) and/or calbindin (CB) [40], we investigated the RC distributions of these three interneuron classes. SST cells were identified as tdTom(+) cells in SST-Ai14 mice (**Figure 3A,** n=7 mice) while PV and CB cells were identified using anti-CB (**Figure 3B**, n=6 mice) or anti-PV immunochemistry (**Figure 3C,** n=6 mice). To quantify interneuron density, somas were counted in L3 along 1 to 1.5 mm (0.1 mm increments) of the RC axis (**Figure 3A1-C1**, ROIs dashed areas). As previously shown [40], the average densities (cells/mm^2) of SST (235 ± 14) and CB cells (174 ± 27) were greater than PV cells (109 ± 9.0, p: 0.0054, KW-test). To investigate RC patterning, densities for each section were normalized to the most rostral section (~2.46 mm from Bregma [41]). For each animal, normalized density versus RC distance was linearly fit to obtain the slope of the change in density per mm^{-1} (**Figure 3A1-C2**, **Table 1**). Only SST-cell densities consistently varied along the RC axis (**Figure 3A1-4, Table 1**). In the majority of mice (n=5/7), linear fits of SST cell density had significantly negative

143 slope values (mean slope: -0.20 ± 0.04, p: 0.002, MWU-test, **Figure 3A4**, **Table 1**), and the average
144 normalized density across all animals (red filled circles, **Figure 3A3**) also decreased (slope: -0.25 ±
145 0.03, p<0.0001). The RC distributions of CB cells were highly variable with individual mice showing
146 increases (n=2, i.e. **Figure 3B1,2**), decreases (n=1) or no change (n=3) along the RC axis. The
147 distribution of CB slopes did not differ from zero (0.13 ± 0.16, p: 0.37, MW-test, **Figure B4**) and the
148 average normalized density did not change with RC distance (slope: 0.11 ± 0.17, p: 0.55, **Figure 3B3**).
149 PV cell density appears to decrease along the RC axis. However, this was only significant in one PV
150 animal (filled black circle, **Figure 3C4, Table 1**) and the average normalized density across all animals
151 (-0.27 ± 0.10, p: 0.031, **Figure 3C3**). In the majority of mice (n=5/6), PV cell density did not significantly
152 vary with RC distance and the distribution of slopes did not differ from zero (-0.16 ± 0.08, p: 0.065, MW-
153 test, open circles, **Figure 3C4**). Altogether, these findings suggest it is unlikely that stronger caudal
154 inhibition of dPCs arises from a rostral-to-caudal increase in interneuron density in L3.

155 We have previously shown that SST-cells inhibit the majority of L3 interneurons in APC [42].
156 This suggests that the high rostral density of SST cells could underlie rostrally-biased inhibition of
157 interneurons. To test this, we selectively expressed ChR2 in SST-cells and repeated grid stimulation
158 while recording IPSCs in L3 interneurons and dPCs (**Figure 4A**). As predicted, SST-cells provided
159 rostrally-biased inhibition to the majority (73%) of L3 interneurons (bias: -0.11 ± 0.04, p: 0.02, n=22,
160 **Figure 4B1,2**). Bias values did not significantly differ between VGAT-ChR2 and SST-ChR2 animals (p:
161 0.69, unpaired t-test). Thus, activating solely SST-cells replicates the rostrally-biased inhibition (I_R: 0.58
162 ± 0.03 > I_C: 0.048 ± 0.03, p: 0.017, paired t-test, **Figure 4D**) of L3 interneurons seen in VGAT-ChR2
163 animals. Interestingly, the strength of SST-mediated inhibition onto L3 interneurons also did not
164 significantly differ (6.82 ± 1.4 pAs) from that in VGAT-ChR2 animals (7.02 ± 0.92 pAs, p: 0.91, unpaired
165 t-test). Although one should be cautious comparing between transgenic lines, one interpretation is that
166 SST cells are a major source of rostrally-biased inhibition onto L3 interneurons.

167 In dPCs, SST-ChR2 mediated inhibition was significantly weaker (4.77 ± 0.89 pAs) than
168 VGAT-ChR2 (8.63 ± 0.84 pAs, p: 0.003, unpaired t-test). This would be expected if SST-cells are only a

169 subset of the interneurons that inhibit dPCs. SST-ChR2 cells provided rostrally-biased inhibition to
170 50% of dPCs (n=7/14, **Figure 4C1**) compared to only 2/16 in VGAT-ChR2 animals. Consequently, the
171 distribution of bias values was not coherently asymmetric and did not differ from zero (0.06 ± 0.08, p:
172 0.45, one sample t-test, n=14, **Figure 4C2**). Finally, in contrast to VGAT-ChR2 activation, SST-ChR2
173 inhibition did not differ between rostral and caudal sites (p: 0.50 paired t-test, **Figure 4D**). Thus,
174 activation of solely SST-cells increases rostrally-biased inhibition of many dPCs and ultimately
175 neutralizes inhibitory bias across the population. These findings are consistent with rostrally-biased
176 distributions of SST-cells and suggest that additional inhibitory circuits are required to produce
177 consistent, caudally biased inhibition of dPCs.

178 There are two ways to produce caudally biased inhibition of dPCs - 1) increase caudal
179 inhibition; or 2) decrease rostral inhibition. We have not found a mechanism to support increased
180 caudal inhibition. However, we have shown that SST-cells provide rostral inhibition to interneurons
181 (**Figure 4B**), which could decrease rostral inhibition of dPCs. To test this possibility, we bred triple
182 transgenic animals that express ChR2 in all interneurons but only SST-cells express the inhibitory
183 DREADD, hM4Di (abbreviated: VGAT-ChR2-SST-Di). In these mice, the DREADD agonist CNO (20
184 μM, bath) reduces SST-cell activity. We performed grid stimulation of L3 sites (**Figure 4E**) and
185 compared IPSC strength and RC bias in control conditions (green) versus CNO (black, **Figure 4F**).
186 Upon application of CNO, IPSC strength decreased consistent with a loss of direct, SST mediated
187 inhibition of dPCs (Control: 4.14 ± 0.70 pAs; CNO: 2.72 ± 0.40 pAs, p: 0.007, paired t-test, n=12). If
188 SST-cells influence caudal bias through rostral disinhibition, we expect a loss in SST-mediated
189 inhibition would shift bias to less caudal values. Surprisingly, the mean bias did not change significantly
190 in CNO (bias: +0.17 ± 0.08, n=12) compared to control (bias: +0.19 ± 0.06, 0.57, paired t-test).
191 However, the bias distribution was significantly asymmetric in control conditions (mean>0, p: 0.010, one
192 sample t-test), whereas in CNO, bias values were not significantly asymmetric (p: 0.051, one sample t-
193 test). This is because caudal bias both increased (n=4/12) and decreased (n=8/12) across the dPC
194 population with CNO application. In a small number of dPCs, increased caudal bias (n=4/12, Δ_{Bias}=

195 $Bias_{CNO}$-$Bias_{Control}$ =+0.13 ± 0.04, gray bars **Figure 4G**) can be explained by a loss of direct, SST-
196 mediated inhibition at rostral sites. In contrast, the majority of dPCs (n=8/12) shifted toward less caudal
197 bias values with CNO (Δ_{Bias} -0.09 ± 0.03, black bars, **Figure 4G**). In these cells, CNO produced a
198 significantly greater reduction in inhibition at caudal sites (-35 ± 9%) versus rostral sites (-24 ± 7%,
199 $p<0.05$, WSR-test, n=8). This suggests that rostral interneurons are normally suppressed by SST-cells
200 in control conditions, but rebound during CNO application and neutralize bias. Thus, caudally biased
201 inhibition of dPCs could arise by rostral disinhibition of PCs through SST-to-interneuron microcircuits.

202 *Rostral-caudal spatial profiles of neural activity*

203 What role might RC patterning of inhibition play in regulating neural activity during olfactory
204 processing? Although odor responsive neurons are distributed in APC, few studies have addressed the
205 spatial patterns of neural activity along the full extent of the APC [22,24,28]. To investigate the RC
206 patterning of neural activity in APC, we used targeted recombination in active populations (TRAP) in
207 $FosCre^{ERT}$ mice [38]. These mice express a tamoxifen-dependent cre-recombinase under the promoter
208 for the activity dependent, immediate early gene *c-fos.* We used $FosCre^{ERT}$x Ai14 mice to express the
209 fluorescent protein, tdTomato in neurons activated in the presence hydroxytamoxifen (4-OHT), (**Figure**
210 **5A, Supplemental Figure 1**). We measured the spatial distribution of active neurons along the RC axis
211 of APC in three conditions: home cage with no odor (HC), home cage with novel odor (HCO), or
212 exploration of a novel environment with novel odor (NEO) (**Figure 5B1,2**). Briefly, HC (n=6) and HCO
213 (n=6) mice were given a single dose of 4-OHT and then returned to the home cage. HCO mice were
214 allowed to rest for 30 min then exposed to odor in the home cage for 30 min. NEO mice (n=6) were
215 given 4-OHT, rested for 30 min, and then explored a novel environment plus odor for 30 min before
216 being returned to the home cage. The novel environment was a divided arena with two cups of
217 bedding- one odorized, one blank- at the end of each arm (**Figure 5B2,** schematic far right). In a
218 subset of mice (n=4), location within the arena was monitored. NEO mice were highly active and
219 sampled both arms as well as the center (C) of the arena throughout exposure period (30 min, **Figure**
220 **5B3**). Mice spent nearly equivalent time per visit in the odorized (8.1 ± 3.5 s) and blank (9.8 ± 3.5 s)

221 arms, but visited the blank arm (49 ± 33 visits) more frequently than the odorized arm (25 ± 14 visits).
222 The majority of HCO and NEO mice were exposed to isoamyl acetate. One cohort of mice (n=2 HCO,
223 n=1 NEO) was exposed to ethyl-butyrate. Results did not differ between odors and were grouped.
224 Following odor exposure, mice remained in their home cages, undisturbed, in the dark for 10-12 hours.
225 Mice were sacrificed 5 days later and tdTom(+) neurons were counted along ~1.5 mm of the RC axis.
226 Neural activity was quantified as the density (cells/mm^2) of tdTom(+) cells in laminar regions of interest
227 (L2, L3 ROIs, **Figure 5A**) located directly under the LOT. Densities were normalized to the most rostral
228 section for linear fits as described for interneuron densities (**Figure 3**). Summary data is presented in
229 **Figure 5** and **Table 2**; representative mice from each group and odor are shown in **Supplemental**
230 **Figure 1**.

231 We found laminar differences in both the average density and the RC spatial pattern of active
232 neurons with odor exposure. In L2, the average density of tdTom(+) neurons (in cells/mm^2) was
233 significantly greater in odor-exposed animals, NEO (243 ± 43) and HCO (199 ± 13), compared to HC
234 animals (113 ± 18, p: 0.013 KW-test, **Figure 5F1**). In L3, average density did not vary with condition
235 (HC: 52 ± 11; HCO: 68 ± 5, and NEO: 76 ± 15, p: 0.149 KW-test, **Figure 5F2**). In contrast, we found
236 RC spatial patterning of neural activity in L3 (**Figure 5D**) but not L2 (**Figure 5C**). The normalized
237 density of tdTom(+) neurons was plotted against RC distance for individual mice (open triangles) and
238 averaged across animals (solid triangles, **Figure 5C,D**). RC patterning was defined as significant non-
239 zero slope values from linear fits of RC densities in individual animals as well as across animals within
240 a group (**Table 2)**. In L2, the distributions of slope values did not significantly differ from zero (HC: 0.39
241 ± 0.27; HCO: -0.01 ± 0.10; NEO: -0.08 ± 0.07 mm^{-1}, p: 0.065 - 0.38, MWU-test, **Figure 5C, Table 2**) or
242 between conditions (p: 0.104 KW-test, **Figure 5E1**). However, in L3, there was significant RC
243 patterning of active neurons that further differed between HC, HCO and NEO conditions (**Figure 5D,**
244 **E2**). All NEO mice showed a significant decrease in the density of active neurons along the RC axis
245 (filled red triangles, slope distribution ≠ 0: -0.45 ± 0.05 mm^{-1}, **p: 0.005, MWU-test, **Figure 5E2, Table**
246 **2**). Further, the distribution of slope values was significantly more negative in NEO mice than HCO or

247 HC (★★, p: 0.0046, KW-test, **Figure 5E2**). Consistent with findings from individual NEO animals, the
248 average change in RC density across animals was also significantly negative (red triangles, -0.47 ±
249 0.04, p<0.000, **Figure 5D3**). In HCO animals, RC patterning was shallower and less reliable in
250 individual mice than NEO animals. The average density across animals decreased significantly with RC
251 distance but the slope was less than half that of NEO animals (gold triangles: -0.19 ± 0.04; p: 0.0005,
252 linear regression, **Figure 5D2**). Further, although the distribution of slopes across mice was significantly
253 non-zero (-0.21 ± 0.12 mm^{-1}, **p: 0.005, MWU-test), RC decreases were rarely significant in individual
254 mice (n=2, filled orange triangles, **Figure 5E2, Table 2**). In HC animals, the average density across
255 animals appears to increase with RC distance (slope: 0.24 ± 0.10 mm^{-1}; p: 0.037, linear regression,
256 **Figure 5D1**). However, in individual animals, the distribution of slopes was inconsistent- positive (n=3),
257 negative (n=2) and neutral (n=1) (**Table 2**) and did not significantly differ from zero (slope: 0.13 ± 0.14
258 mm^{-1}, **Figure 5E2**). Finally, across conditions, changes tdTom(+) densities do not correlate with
259 changes in the total number of cells along the RC axis. In 6 mice, two from each group (NEO, HCO,
260 HC) we quantified the RC density of all cells (DAPI stain) in L2 and L3 **(Supplemental Figure 2**). Total
261 cells consistently increased along the RC axis in L2 (slope distribution ≠ 0: 0.54 ± 0.21 mm^{-1}, p: 0.0051
262 MWU) but not in L3 (0.08 ± 0.11 mm^{-1}, p: 0.94 MWU, n=6). To summarize, we show that odor exposure
263 increases the density of active neurons in L2 but not L3, and significantly changes the RC spatial
264 patterning of neural activity in L3 but not L2. The lack of consistent, significant RC patterning in
265 individual mice in HC and HCO animals, suggests that spatial patterning within APC is not a reliable
266 feature of odor processing in familiar environments. In contrast, exploration of a novel odor environment
267 (NEO) strongly and reliably changes RC spatial patterning in L3 compared to HCO, and HC contexts.
268 This suggests that space may be an avenue to differentially process odor information depending on
269 context.

270 In the first section of this study, we show that inhibition of dPCs in L3 increases along the
271 rostral-caudal axis on the spatial scale of millimeters. We find that a disinhibitory circuit mediated by
272 SST-cells supports this gradient through rostrally-biased inhibition of interneurons (**Figure 6A**). Could

273 these RC asymmetries in inhibition play a role in the RC patterning of neural activity in L3 during odor
274 exposure? In NEO animals, neural activity in L3 decreases from rostral to caudal APC over a spatial
275 scale of millimeters (**Figure 5D2**) comparable to that of increasing inhibition in dPCs (**Figure 1F**). In
276 **Figure 6B,** we plot the average normalized decrease in active L3 neurons in NEO mice and the
277 average normalized increase in inhibition of dPCs along the RC axis. We find that the spatial scales of
278 neural activity and inhibition are well matched with opposing slopes (NEO: slope -0.47 ± 0.04 mm^{-1}, R:
279 0.94, $p<0.0001$; Inhibition: slope 0.67 ± 0.06 mm^{-1}, R: 0.98, p: 0.0001). Thus, when inhibition is
280 weakest, neural activity is maximal (rostral) and when inhibition is strongest, neural activity is minimal
281 (caudal). These findings suggest that inhibitory circuitry could underlie RC patterning of neural activity
282 in L3 of APC. Further, the recruitment of inhibitory gradients and may depend on the context of odor
283 experience. In contrast, inhibition is weaker in L2 where the spatial profiles of neural activity are
284 approximately uniform in L2 and do not seem to vary with odor context. Altogether, these laminar and
285 RC differences in inhibition and neural activity suggest spatially dependent and independent
286 mechanisms work in parallel during odor processing in APC.

287 **Discussion**

288 In this study, we demonstrate rostral-caudal spatial patterning in inhibitory circuitry and neural
289 activity in APC. Our findings reproduce earlier studies that have shown caudally-biased asymmetric
290 inhibition of PCs [32] and a RC decline in fos(+) neurons following odor exposure [22]. However, the
291 underlying circuitry and functional significance of these findings are unknown. Here, we provide three
292 major advances. First, we describe a disinhibitory circuit mediated by SST-cells that decreases rostral
293 inhibition relative to caudal inhibition in L3 PCs. Second, we show that RC patterning of neural activity
294 is confined to L3 and differs with odor exposure in familiar (HCO) versus novel (NEO) contexts. Finally,
295 the density of active neurons decreases along the RC axis following odor exposure in the NEO context
296 commensurate with increasing inhibition of L3 PCs. Specifically, rostral PCs are more active and
297 receive significantly less inhibition (disinhibited) whereas caudal PCs receive stronger inhibition and are

298 less active. Altogether, our findings provide new evidence for RC spatial organization within APC as
299 well as a potential circuit mechanism for varying olfactory processing in different contexts.

300 *Disinhibition by Somatostatin Interneurons*

301 Inhibition plays a critical role in the processing and representation of sensory information in the cortex
302 [43]. In APC, inhibition balances excitation [39,44,45], narrows synaptic integration windows [20,44-48], supports
303 oscillatory activity and sharpens odor tuning [23,49-51]. Despite the prominent role inhibition plays in
304 shaping cortical responses, few studies have addressed circuits that modulate inhibition in APC [49,51]. In
305 neocortex, a number of disinhibitory circuits have been implicated in the gating or tuning of cortical
306 responses to sensory stimuli [52-59]. For example, SST-cells inhibit a range of interneuron classes
307 including fast-spiking, PV interneurons both in neocortex [56,57] and APC [42,51]. In this study, we show that
308 SST interneurons provide rostrally-biased inhibition to L3 interneuron and thus, mediate rostral
309 disinhibition of PCs. Disrupting this disinhibitory circuit through selective optogenetic activation or
310 chemogenetic inhibition of SST cells neutralizes the caudally-biased inhibitory gradient onto dPCs.
311 These findings suggest that SST-cells both inhibit [42] and disinhibit PCs in APC and play a role in the
312 RC patterning of inhibition.

313 Recent studies have shown that SST interneuron activity is modulated in different contexts. In
314 sensory neocortices, SST-cell activity is enhanced by cholinergic modulation [56,60,61], running during
315 visual sensory stimulation [62], or engagement in an auditory task [61]. In somatosensory cortex, whisking
316 specifically increases the firing rates of fast-spiking, SST-cells that preferentially inhibit PV cells [56,59].
317 Likewise, we have shown that two-thirds of SST cells in APC are FS and strongly inhibit PV-like cells [42].
318 Given that sniffing and whisking are correlated [63,64], an intriguing possibility is that actively exploring
319 (running, sniffing and whisking) a novel odor environment (NEO) globally enhances SST-cell activity in
320 sensory cortices. We propose that in APC, enhanced SST-cell activity gates rostral disinhibition and
321 increases in rostral neural activity in NEO animals. This interpretation is consistent with recent studies
322 that show interactions between interneurons in network models [65] promote context dependent changes
323 in network activity [58,61].

324 *Spatial patterning of neural activity in APC.*

325 The spatial patterning is difficult to investigate *in vivo* due to the extent (~1.5 mm) and ventral location
326 of APC. Population imaging shows minimal spatial variation in response to different odors or intensities,
327 but typically only sample L2 neurons across ~300 µm of the RC axis [25-27]. Multi-site unit recordings
328 broadly sample the RC axis and suggest RC variation in odor-evoked firing rates [24] but sample a small
329 proportion of neurons per region. Likewise, intrinsic signal imaging or local field potential (LFP)
330 recordings broadly sample the RC axis and suggest systematic variation along the RC-axis in
331 concentration thresholds [28] and oscillatory activity respectively [13,29,30,66]. But these tools lack the fine
332 resolution to identify the neural circuits contributing to these responses.

333 To investigate the spatial profiles neural activity *in vivo*, we used TRAP-mice that conditionally
334 express of cre-recombinase linked to the IEG, *c-fos* [38]. This tool provides sufficient spatial scale to
335 investigate population activity along the entire RC axis at a resolution amenable microcircuit analysis.
336 TRAP-mice are advantageous over traditional IEG methods because cre-recombinase promotes
337 continuous cytoplasmic expression of tdTom independent of initial strength of activation. The limitation
338 is that the temporal window for capturing activity is longer. Labeling is optimal within one hour of 4-
339 OHT injection and declines significantly ~6 hours post injection [38,67]. Thus, neural densities are
340 expected to be higher in TRAP animals due to enhanced labeling of weak responses and potential
341 spurious labeling over long time windows. To minimize the latter, animals were undisturbed in the dark
342 for 10h following exposure and HC animals provided a baseline for handling and non-specific labeling.

343 Consistent with previous IEG immunolabeling [22,68,69], the density of activated, TRAP-tdTom(+)
344 cells increases significantly in odor-exposed animals (HCO and NEO) compared to HC animals. We
345 find these changes in density are restricted to L2 whereas RC patterning of neural activity occurs in L3.
346 A lack of RC patterning in L2 was initially surprising since L2 sPCs also receive caudally-biased
347 inhibition. However, L2 sPCs receive weaker inhibition than L3 dPCs [39] while L2 semilunar cells and
348 interneurons do not receive asymmetric inhibition. This suggests that the uniformly distributed spatial
349 pattern of neural activity in L2 is inherited from the spatial profile of afferent and/or recurrent excitation
350 [18-20]. In contrast, interneuron densities, particularly SST cells, are greatest in L3 [40,42]. We show that
351 individual L3 dPCs receive strong inhibition that increases with caudal position along the RC axis with

352 the same spatial scale as decreases in neural activity. These are ideal conditions for inhibition to
353 dictate L3 RC activity patterns. Altogether, laminar differences in inhibition and RC patterning coincide
354 with layer-specific differences PC subclasses and projection targets [70,71] and support the premise that
355 parallel processing streams exist in APC.

356 *Functional roles for RC asymmetries in olfactory processing*

357 Given the seemingly uniform profile of excitation in APC, a surprising finding is that inhibitory
358 strength increases along the rostral-caudal axis. In entorhinal cortex, a dorsal-ventral inhibitory gradient
359 coincides with an increase in PV interneuron density, changes in receptive field size and increased
360 gamma oscillatory power [72]. We find SST cells rather than PV cells change in density along the RC
361 axis. Since SST-cell inhibition has a subtractive effect on PC odor tuning [51], it is possible that SST-
362 mediated inhibition of PCs supports changes in odor tuning across the RC extent of APC. Alternatively,
363 RC patterning of inhibition and neural activity could bias projections from rostral versus caudal APC in
364 different contexts. For example, higher rostral activity during NEO exploration could preferentially
365 increase feedback to the OB [73] or output to the OFC [11,33]. Finally, RC variation in inhibition may also
366 interact with other RC asymmetries to affect the spatial profiles of neural activity in APC. For example,
367 tufted cells afferents are limited to the rostral-ventral APC [18] and the overall density of OB afferents
368 decreases along the RC extent of the LOT. Likewise, projections from PPC [74] and frontal cortex [11,34]
369 also show RC biases. It remains to be determined if the various sources of RC asymmetry work in
370 concert during olfactory processing. Nonetheless, our study adds to a growing body of evidence that,
371 despite the lack of a topographic code for odor identity, space is a relevant dimension in olfactory
372 processing in piriform cortex.

373

374 **Methods**

375 *Animals:* A number of transgenic mouse lines and crosses were used in this study. VGAT-ChR2 mice
376 (*VGAT-Chr2:* B6.Cg-Tg(Slc32a1-COP4*H134R/EYFP)8Gfng/J) express channelrhodopsin in all

377 interneurons [75]. The *SST-Cre* (B6:Sst<tm2.1(cre)Zjh>/J) mice were crossed with *Ai32 mice* (B6:129S-
378 Gt(ROSA)26Sortm32(CAG-COP4*H134R/EYFP)Hze/J) or DREADDi mice (B6N.129-
379 *Gt(ROSA)26Sortm1(CAG-CHRM4*,-mCitrine)Ute*/J) to express channelrhodopsin or the inhibitory
380 DREADD, hM4Di [37]. TRAP mice (FosCre^{ERT}: (B6.129(Cg)-Fos(tm1.1(cre/ERT2)Luo/J) were crossed
381 with Ai14 (B6.Cg-*Gt(ROSA)26Sortm14 (CAG-tdTomato)Hze*/J) to conditionally express tdtomato [38]. All
382 mice are from Jackson Laboratories. Mice were housed in groups of 2-5 animals on a 10:14 light/dark
383 cycle unless otherwise stated. All experiments involved mice of both sexes and age ranges from P20-
384 P300 as indicated.

385 *Slice preparation:* Brain slices of anterior piriform cortex (APC) were prepared from mice aged P19-35.
386 The mice were anesthetized with isoflurane and decapitated. The brain was removed from the skull
387 and immersed in ice cold oxygenated (95% O_2-5% CO_2) ACSF (in mM: 125 NaCl, 2.5 KCl, 25 $NaHCO_3$,
388 1.25 NaH_2PO_4, 1.0 $MgCl_2$, 25 Dextrose, 2.5 $CaCl_2$) (all chemicals from Sigma, USA unless otherwise
389 stated). Parasagittal slices (300 μm) were made using a vibratome (Leica Biosystems) in ice cold
390 ACSF. The slices were transferred to warm ACSF (37°C) for 30 min and then rested at 20-22°C for 1
391 hour prior to recording (31-35°C). All surgical procedures were approved by the University of Pittsburgh
392 IACUC.

393 *Electrophysiology*: Whole cell, voltage and current clamp recordings were performed using a
394 MultiClamp 700B amplifier (Molecular Devices, Union City, CA). Data were low pass filtered (4 kHz)
395 and digitized at 10 kHz using an ITC-18 (Instrutech) controlled by custom software (Recording Artist,
396 https://bitbucket.org/rgerkin/recording-artist) written in IgorPro (Wavemetrics). Recording pipettes (4-10
397 MΩ) were pulled from borosilicate glass (1.5 mm, outer diameter) on a Flaming/Brown micropipette
398 puller (Sutter Instruments). The series resistance (<20 MΩ) was not corrected. The intracellular
399 solution consisted of (in mM) 130 K-gluconate, 5 KCl, 2 $MgCl_2$, 4 ATP-Mg, 0.3 GTP, 10 HEPES, and 10
400 phosphocreatine, 0.05% biocytin, 4.5 μM QX-314. Recordings were obtained from L2/3 pyramidal cells
401 (PCs), L2 semilunar (SL) cells as well as interneurons in L2/3. Neurons were visualized using infrared-
402 differential interference contrast microscopy (IR-DIC, Olympus). In transgenic mice, interneurons were

403 targeted using fluorescence (YFP) and PCs as the absence of fluorescence. For all neurons, intrinsic
404 subthreshold properties such as input resistance, and time constant were assessed using a series of
405 hyperpolarizing and depolarizing current steps (-50 pA to 50 pA, 1 s duration). Neural identity was
406 confirmed post hoc using intrinsic properties and anatomical analysis of biocytin fills.

407 *Light stimulation:* Blue light (λ=460-488 nm, GFP block, Olympus) for optical stimulation was provided
408 by metal halide lamp (200W, Prior Scientific) passed through the microscope objective (60x, immersion,
409 Olympus). Light pulses were controlled using a mechanical shutter (Sutter Instruments). The light spot
410 was restricted to a ~70 μm diameter (0.5 mW) using the minimum aperture. To obtain the spatial profile
411 of inhibition, interneurons were focally activated in a 5x4 grid pattern while IPSCs were recorded in
412 interneurons or PCs. The horizontal axis of the grid was centered on the recorded neuron with
413 stimulation sites ranging from -300 μm (rostral) to +300 μm (caudal) at 150 μm increments. The vertical
414 axis ranged L1 to L3 in 125 μm increments corresponding to different lamina. Each grid site was
415 stimulated with 2 light pulses (20 ms duration, 100 ms interpulse interval, 15 s between trials). The 20
416 ms duration was chosen to reliably evoke least one spike and rarely 2 spikes in response to a single
417 pulse of direct somatic stimulation using the 70 μ spot at 0.5 mW [39]. Grids were repeated 3-7 times per
418 neuron and each grid site was stimulated once every 6 min. Since solely inhibitory neurons are
419 activated and there is little evidence of depolarizing inhibition, polysynaptic responses are unlikely
420 under these recording conditions.

421 *CNO Application*: Stock solutions (10 mM in 0.9% saline) of the DREADD agonist, Clozapine-N-oxide
422 (CNO), were made fresh for each cohort of animals, aliquoted and stored at -20°C for up to 2 weeks.
423 On the day of experiment, CNO stock was diluted (20 μM in ACSF) for bath application.

424 *Analysis of inhibition:* Electrophysiology traces of IPSCs are presented as the average across trials
425 (n=3-7) for individual neurons. IPSC strength was taken as the area (pAs) under the first IPSC of the
426 pair of light pulses. The second IPSC was not analyzed due to unreliable AP firing on the second light
427 pulse [39]. Average PSCs with minimum amplitude of 10 pA were included for analyses; smaller PSCs
428 were not distinguishable from noise and given a value of 0. To compare the spatial profiles of inhibition

429 across animals IPSC amplitudes were normalized to the strength of the maximum IPSC regardless of
430 location in the grid. The rostral-caudal bias was taken as the average normalized inhibition from the
431 caudal sites minus the average inhibition of the rostral sites, divided by the summed inhibition from both
432 sides. The bias metric ranges from -1 (rostral bias) to +1 (caudal bias). Since L1 inhibition was typically
433 weak [39] these sites were excluded from the bias metric.

434 *TRAP-mice:* To label active neurons during odor exposure, we used TRAP mice. Briefly, FosCre^{ERT}
435 mice express a tamoxifen-dependent cre-recombinase under the promoter for the activity dependent,
436 immediate early gene *c-fos*. FosCre^{ERT} mice were crossed with Ai14 mice and the offspring
437 conditionally express tdTomato (tdTom) in active neurons upon tamoxifen administration. We used 4-
438 hydroxytamoxifen (4-OHT) (Sigma) because the time window of activation was faster and narrower
439 than tamoxifen [38]. Doses of 4-OHT were freshly made on the day of injection. Briefly, 4-OHT (15 mg)
440 was dissolved in in 100% ethanol (200µl) by sonication at 37°C (~1 hr). Then peanut oil (1.5 ml, Sigma)
441 was added and ethanol was removed via centrifugation (15 min) and vacuum evaporation (1-2 hrs).
442 The final solution (50mg/kg) was filtered (0.2 µm) and administered by intraperitoneal injection (~150-
443 200 µl per animal) 30 min before odor exposure.

444 *Odor exposure and behavior:* There were three groups of TRAP-mice (P90-300): 1) home cage
445 animals (HC), 2) home cage plus odor (HCO), and 3) novel environment plus odor (NEO). Experiments
446 were done serially, with 3-4 mice per cohort. In each cohort, there was typically at least one mouse per
447 condition. However, there were losses due to death (n=2), poor perfusion (n=2) and insufficient 4-OHT
448 dosage (n=3). Whenever possible, mice from the same litter were used for each cohort or nearly age-
449 matched litters (± 1 week) were used. Mice were singly housed on a 12:12 light/dark cycle and all
450 testing was done ±1 hr from the onset of the dark cycle. Mice were food restricted (90% body weight)
451 as well as handled and weighed daily for 3 days prior to 4-OHT injection and odor exposure. Odor
452 stimuli were isoamyl acetate (Sigma) or ethyl butyrate (Sigma) at 1:100 dilution in mineral oil. For HCO
453 animals, 100 µl of odor was applied to a cotton ball in an open tube that was placed in the cage for 30
454 min. For NEO mice, filter paper (0.5 x 0.5 cm) was saturated with odor and then buried in a paper cup

455 filled with clean bedding. To encourage exploration, the cup of odorized bedding was placed at the end
456 of one arm of a divided arena (20 x 10 inches) and a blank cup of bedding in the other arm (**Figure**
457 **5B2)**. Following 4-OHT administration and exposure, animals were returned to their home cages and
458 undisturbed in the dark for 10-12 hours. Mice were sacrificed 5 days post 4-OHT and neural activity in
459 each context was quantified as the density of tagged, tdTom(+) neurons in L2 and L3 of APC. The
460 average densities of tdTom cells across L2/3 ranged from ~70-400 cells/mm^2 depending on condition.
461 A minimum average density of 30 cells/mm^2 was set as a lower threshold for inclusion of an animal in
462 the data set. In three excluded animals, densities were <10 cells/mm^2 suggesting that 4-OHT dosage
463 was insufficient.

464 *Anatomy*: Mice were given an overdose of ketamine-xylazine. Mice were then perfused transcardially
465 (20 ml/min) with 0.1 M sodium phosphate buffer (PB), followed by 200 ml of 4% paraformaldehyde
466 (PFA) in 0.2M PB. Brains were removed and fixed in 4% PFA overnight at 4°C, then transferred to a
467 sucrose solution. Coronal slices (50 µm) were cut using a freezing microtome maintained in phosphate
468 buffer prior to immunochemistry (anti-PV or anti-CB staining) and/or mounting. Parvalbumin (PV) cells
469 were immunostained using rabbit anti-parvalbumin (PV27, Swant, 1:1000). Calbindin cells were
470 immunostained using rabbit anti-calbindin D-28K (CB38, Swant, 1:1000). In both cases, the secondary
471 was donkey anti-rabbit Alexa-fluor-488 (#A21206 Life Technologies, 1:500). Every other section was
472 mounted using fluoromount to protect fluorescence and minimize background. Sections were imaged
473 on a Nikon Eclipse-Ci microscope at 4x magnification. Illumination was provided by a mercury lamp
474 (Nikon Intensilight) and delivered through appropriate filter blocks for GFP (495 nm) and tdTomato (585
475 nm). Light intensity and exposure duration (100-400 ms) were optimized for the first section in a series
476 using automated software (Nikon Elements), then maintained for ensuing sections. Sections were
477 photographed using a CCD HD color camera (Nikon DsFi2).

478 *Cell counts*: Neural densities were quantified as number of cells per mm^2 in laminar regions of interest
479 (ROI) located directly under the lateral olfactory tract in APC. Counts were made in a single focus plane
480 (4x magnification) for each section chosen to maximize the number of cells in focus. Automated counts

of somas were obtained based on fluorescence intensity and circularity using Elements Software (Nikon). Two researchers independently verified all counts with at least one blind to condition. In the event of discrepancy, a third individual, blind to condition, performed counts. Every other coronal section (8-15 sections per animal) was analyzed spanning 1-1.5 mm along the rostral-caudal extent of the APC. The average density was taken across all sections in a given animal. To assess rostral-caudal spatial patterning, densities in each section were normalized to the most rostral section corresponding to ~2.46 mm from Bregma [41]. For each animal, the slope of the least-squares linear regression between normalized density and RC distance was used to quantify spatial patterning.

Statistics: All data is presented as mean ± SE unless otherwise stated. Initial sample sizes were determined based on previous studies [22, 57] using comparable techniques and statistical comparisons. Power analyses were conducted following statistical analysis to ensure sufficient power (Supplemental Tables 1,2,3). Statistical tests were performed using two tailed, one or two-sample, paired or unpaired Student's t-test as appropriate. In cases of small sample sizes (<10) non-parametric tests were used, including the Mann-Whitney U-test (MWU) for unpaired data and the Wilcoxon Signed Ranks test (WSR) for paired data. For multiple comparisons we used ANOVA with post hoc Tukey Test (ANOVA-Tukey). For groups with small sample sizes multiple comparisons were made using non-parametric, Kruskal-Wallis tests (KW-test). All statistical tests are indicated in the main text and/or figure legends.

Acknowledgements: We thank Brent Doiron and Nathan Urban for helpful comments on this study and manuscript. We thank Samantha Mielo for technical support. This work was supported by a National Institute on Deafness and Other Communication Disorders Grant (R01 DC015139) to AMMO and an RK Mellon Fellowship to AML.

Author Contributions: AML and AMMO designed the project, collected and analyzed electrophysiological and anatomical data, and wrote the manuscript. NWV collected and analyzed electrophysiological data. MCB, and PS collected and analyzed anatomical data.

508 **References**

509 1. Mombaerts, P., Wang, F., Dulac, C., Chao, S.K., Nemes, A., Mendelsohn, M., Edmondson, J. & Axel, R.
510 Visualizing an olfactory sensory map. *Cell* **87**, 675-86 (1996).
511 2. Mori, K. & Sakano, H. How is the olfactory map formed and interpreted in the mammalian brain? *Annu*
512 *Rev Neurosci* **34**, 467-99 (2011).
513 3. Buonviso, N., Chaput, M.A. & Scott, J.W. Mitral cell-to-glomerulus connectivity: an HRP study of the
514 orientation of mitral cell apical dendrites. *J Comp Neurol* **307**, 57-64 (1991).
515 4. Davison, I.G. & Ehlers, M.D. Neural circuit mechanisms for pattern detection and feature combination in
516 olfactory cortex. *Neuron* **70**, 82-94 (2011).
517 5. Davison, I.G. & Katz, L.C. Sparse and selective odor coding by mitral/tufted neurons in the main olfactory
518 bulb. *J Neurosci* **27**, 2091-101 (2007).
519 6. Fried, H.U., Fuss, S.H. & Korsching, S.I. Selective imaging of presynaptic activity in the mouse olfactory
520 bulb shows concentration and structure dependence of odor responses in identified glomeruli. *Proc Natl*
521 *Acad Sci U S A* **99**, 3222-7 (2002).
522 7. Soucy, E.R., Albeanu, D.F., Fantana, A.L., Murthy, V.N. & Meister, M. Precision and diversity in an odor
523 map on the olfactory bulb. *Nat Neurosci* **12**, 210-20 (2009).
524 8. Spors, H., Wachowiak, M., Cohen, L.B. & Friedrich, R.W. Temporal dynamics and latency patterns of
525 receptor neuron input to the olfactory bulb. *J Neurosci* **26**, 1247-59 (2006).
526 9. Willhite, D.C., Nguyen, K.T., Masurkar, A.V., Greer, C.A., Shepherd, G.M. & Chen, W.R. Viral tracing
527 identifies distributed columnar organization in the olfactory bulb. *Proc Natl Acad Sci U S A* **103**, 12592-7
528 (2006).
529 10. Haberly, L.B. & Price, J.L. Association and commissural fiber systems of the olfactory cortex of the rat. *J*
530 *Comp Neurol* **178**, 711-40 (1978).
531 11. Illig, K.R. Projections from orbitofrontal cortex to anterior piriform cortex in the rat suggest a role in
532 olfactory information processing. *J Comp Neurol* **488**, 224-31 (2005).
533 12. Majak, K., Ronkko, S., Kemppainen, S. & Pitkanen, A. Projections from the amygdaloid complex to the
534 piriform cortex: A PHA-L study in the rat. *J Comp Neurol* **476**, 414-28 (2004).
535 13. Chabaud, P., Ravel, N., Wilson, D.A. & Gervais, R. Functional coupling in rat central olfactory pathways: a
536 coherence analysis. *Neurosci Lett* **276**, 17-20 (1999).
537 14. Gottfried, J.A., Winston, J.S. & Dolan, R.J. Dissociable codes of odor quality and odorant structure in
538 human piriform cortex. *Neuron* **49**, 467-79 (2006).
539 15. Kadohisa, M. & Wilson, D.A. Separate encoding of identity and similarity of complex familiar odors in
540 piriform cortex. *Proc Natl Acad Sci U S A* **103**, 15206-11 (2006).
541 16. Litaudon, P., Amat, C., Bertrand, B., Vigouroux, M. & Buonviso, N. Piriform cortex functional
542 heterogeneity revealed by cellular responses to odours. *Eur J Neurosci* **17**, 2457-61 (2003).
543 17. Ghosh, S., Larson, S.D., Hefzi, H., Marnoy, Z., Cutforth, T., Dokka, K. & Baldwin, K.K. Sensory maps in the
544 olfactory cortex defined by long-range viral tracing of single neurons. *Nature* **472**, 217-20 (2011).
545 18. Igarashi, K.M., Ieki, N., An, M., Yamaguchi, Y., Nagayama, S., Kobayakawa, K., Kobayakawa, R., Tanifuji,
546 M., Sakano, H., Chen, W.R. & Mori, K. Parallel mitral and tufted cell pathways route distinct odor
547 information to different targets in the olfactory cortex. *J Neurosci* **32**, 7970-85 (2012).
548 19. Sosulski, D.L., Bloom, M.L., Cutforth, T., Axel, R. & Datta, S.R. Distinct representations of olfactory
549 information in different cortical centres. *Nature* **472**, 213-6 (2011).
550 20. Franks, K.M., Russo, M.J., Sosulski, D.L., Mulligan, A.A., Siegelbaum, S.A. & Axel, R. Recurrent circuitry
551 dynamically shapes the activation of piriform cortex. *Neuron* **72**, 49-56 (2011).
552 21. Yang, J., Litscher, G., Sun, Z., Tang, Q., Kishi, K., Oda, S., Takayanagi, M., Sheng, Z., Liu, Y., Guo, W.,
553 Zhang, T., Wang, L., Gaischek, I., Litscher, D., Lippe, I.T. & Kuroda, M. Quantitative analysis of axon
554 collaterals of single pyramidal cells of the anterior piriform cortex of the guinea pig. *BMC Neurosci* **18**, 25
555 (2017).

22. Illig, K.R. & Haberly, L.B. Odor-evoked activity is spatially distributed in piriform cortex. *J Comp Neurol* **457**, 361-73 (2003).
23. Poo, C. & Isaacson, J.S. Odor representations in olfactory cortex: "sparse" coding, global inhibition, and oscillations. *Neuron* **62**, 850-61 (2009).
24. Rennaker, R.L., Chen, C.F., Ruyle, A.M., Sloan, A.M. & Wilson, D.A. Spatial and temporal distribution of odorant-evoked activity in the piriform cortex. *J Neurosci* **27**, 1534-42 (2007).
25. Roland, B., Deneux, T., Franks, K.M., Bathellier, B. & Fleischmann, A. Odor identity coding by distributed ensembles of neurons in the mouse olfactory cortex. *Elife* **6**(2017).
26. Stettler, D.D. & Axel, R. Representations of odor in the piriform cortex. *Neuron* **63**, 854-64 (2009).
27. Tantirigama, M.L., Huang, H.H. & Bekkers, J.M. Spontaneous activity in the piriform cortex extends the dynamic range of cortical odor coding. *Proc Natl Acad Sci U S A* **114**, 2407-2412 (2017).
28. Sugai, T., Miyazawa, T., Fukuda, M., Yoshimura, H. & Onoda, N. Odor-concentration coding in the guinea-pig piriform cortex. *Neuroscience* **130**, 769-81 (2005).
29. Freeman, W.J. Distribution in time and space of prepyriform electrical activity. *J Neurophysiol* **22**, 644-65 (1959).
30. Litaudon, P. & Cattarelli, M. Piriform cortex late activity revealed functional spatial heterogeneity. *Neuroreport* **6**, 1377-80 (1995).
31. Litaudon, P., Datiche, F. & Cattarelli, M. Optical recording of the rat piriform cortex activity. *Prog Neurobiol* **52**, 485-510 (1997).
32. Luna, V.M. & Pettit, D.L. Asymmetric rostro-caudal inhibition in the primary olfactory cortex. *Nat Neurosci* **13**, 533-5 (2010).
33. Chen, C.F., Zou, D.J., Altomare, C.G., Xu, L., Greer, C.A. & Firestein, S.J. Nonsensory target-dependent organization of piriform cortex. *Proc Natl Acad Sci U S A* **111**, 16931-6 (2014).
34. Datiche, F. & Cattarelli, M. Reciprocal and topographic connections between the piriform and prefrontal cortices in the rat: a tracing study using the B subunit of the cholera toxin. *Brain Res Bull* **41**, 391-8 (1996).
35. Ekstrand, J.J., Domroese, M.E., Johnson, D.M., Feig, S.L., Knodel, S.M., Behan, M. & Haberly, L.B. A new subdivision of anterior piriform cortex and associated deep nucleus with novel features of interest for olfaction and epilepsy. *J Comp Neurol* **434**, 289-307 (2001).
36. Boyden, E.S., Zhang, F., Bamberg, E., Nagel, G. & Deisseroth, K. Millisecond-timescale, genetically targeted optical control of neural activity. *Nat Neurosci* **8**, 1263-8 (2005).
37. Zhu, H. & Roth, B.L. DREADD: a chemogenetic GPCR signaling platform. *Int J Neuropsychopharmacol* **18**(2014).
38. Guenthner, C.J., Miyamichi, K., Yang, H.H., Heller, H.C. & Luo, L. Permanent genetic access to transiently active neurons via TRAP: targeted recombination in active populations. *Neuron* **78**, 773-84 (2013).
39. Large, A.M., Vogler, N.W., Mielo, S. & Oswald, A.M. Balanced feedforward inhibition and dominant recurrent inhibition in olfactory cortex. *Proc Natl Acad Sci U S A* **113**, 2276-81 (2016).
40. Suzuki, N. & Bekkers, J.M. Inhibitory neurons in the anterior piriform cortex of the mouse: classification using molecular markers. *J Comp Neurol* **518**, 1670-87 (2010b).
41. Franklin, K. & Paxinos, G. *The Mouse Brain in Stereotaxic Coordinates* (Academic Press, 2007).
42. Large, A.M., Kunz, N.A., Mielo, S.L. & Oswald, A.M. Inhibition by Somatostatin Interneurons in Olfactory Cortex. *Front Neural Circuits* **10**, 62 (2016).
43. Isaacson, J.S. & Scanziani, M. How inhibition shapes cortical activity. *Neuron* **72**, 231-43 (2011).
44. Sheridan, D.C., Hughes, A.R., Erdelyi, F., Szabo, G., Hentges, S.T. & Schoppa, N.E. Matching of feedback inhibition with excitation ensures fidelity of information flow in the anterior piriform cortex. *Neuroscience* **275**, 519-30 (2014).
45. Suzuki, N. & Bekkers, J.M. Distinctive classes of GABAergic interneurons provide layer-specific phasic inhibition in the anterior piriform cortex. *Cereb Cortex* **20**, 2971-84 (2010a).
46. Luna, V.M. & Schoppa, N.E. GABAergic circuits control input-spike coupling in the piriform cortex. *J Neurosci* **28**, 8851-9 (2008).

47. Stokes, C.C. & Isaacson, J.S. From dendrite to soma: dynamic routing of inhibition by complementary interneuron microcircuits in olfactory cortex. *Neuron* **67**, 452-65 (2010).
48. Suzuki, N. & Bekkers, J.M. Microcircuits mediating feedforward and feedback synaptic inhibition in the piriform cortex. *J Neurosci* **32**, 919-31 (2012).
49. Birjandian, Z., Narla, C. & Poulter, M.O. Gain control of gamma frequency activation by a novel feed forward disinhibitory loop: implications for normal and epileptic neural activity. *Front Neural Circuits* **7**, 183 (2013).
50. Poo, C. & Isaacson, J.S. A major role for intracortical circuits in the strength and tuning of odor-evoked excitation in olfactory cortex. *Neuron* **72**, 41-8 (2011).
51. Sturgill, J.F. & Isaacson, J.S. Somatostatin cells regulate sensory response fidelity via subtractive inhibition in olfactory cortex. *Nat Neurosci* **18**, 531-5 (2015).
52. Fu, Y., Kaneko, M., Tang, Y., Alvarez-Buylla, A. & Stryker, M.P. A cortical disinhibitory circuit for enhancing adult plasticity. *Elife* **4**, e05558 (2015).
53. Fu, Y., Tucciarone, J.M., Espinosa, J.S., Sheng, N., Darcy, D.P., Nicoll, R.A., Huang, Z.J. & Stryker, M.P. A cortical circuit for gain control by behavioral state. *Cell* **156**, 1139-52 (2014).
54. Lee, S., Kruglikov, I., Huang, Z.J., Fishell, G. & Rudy, B. A disinhibitory circuit mediates motor integration in the somatosensory cortex. *Nat Neurosci* **16**, 1662-1670 (2013).
55. Letzkus, J.J., Wolff, S.B., Meyer, E.M., Tovote, P., Courtin, J., Herry, C. & Luthi, A. A disinhibitory microcircuit for associative fear learning in the auditory cortex. *Nature* **480**, 331-5 (2011).
56. Munoz, W., Tremblay, R., Levenstein, D. & Rudy, B. Layer-specific modulation of neocortical dendritic inhibition during active wakefulness. *Science* **355**, 954-959 (2017).
57. Pfeffer, C.K., Xue, M., He, M., Huang, Z.J. & Scanziani, M. Inhibition of inhibition in visual cortex: the logic of connections between molecularly distinct interneurons. *Nat Neurosci* **16**, 1068-76 (2013).
58. Pi, H.J., Hangya, B., Kvitsiani, D., Sanders, J.I., Huang, Z.J. & Kepecs, A. Cortical interneurons that specialize in disinhibitory control. *Nature* **503**, 521-4 (2013).
59. Xu, H., Jeong, H.Y., Tremblay, R. & Rudy, B. Neocortical somatostatin-expressing GABAergic interneurons disinhibit the thalamorecipient layer 4. *Neuron* **77**, 155-67 (2013).
60. Chen, N., Sugihara, H. & Sur, M. An acetylcholine-activated microcircuit drives temporal dynamics of cortical activity. *Nat Neurosci* **18**, 892-902 (2015).
61. Kuchibhotla, K.V., Gill, J.V., Lindsay, G.W., Papadoyannis, E.S., Field, R.E., Sten, T.A., Miller, K.D. & Froemke, R.C. Parallel processing by cortical inhibition enables context-dependent behavior. *Nat Neurosci* **20**, 62-71 (2017).
62. Pakan, J.M., Lowe, S.C., Dylda, E., Keemink, S.W., Currie, S.P., Coutts, C.A. & Rochefort, N.L. Behavioral-state modulation of inhibition is context-dependent and cell type specific in mouse visual cortex. *Elife* **5**(2016).
63. Deschenes, M., Kurnikova, A., Elbaz, M. & Kleinfeld, D. Circuits in the Ventral Medulla That Phase-Lock Motoneurons for Coordinated Sniffing and Whisking. *Neural Plast* **2016**, 7493048 (2016).
64. Kurnikova, A., Moore, J.D., Liao, S.M., Deschenes, M. & Kleinfeld, D. Coordination of Orofacial Motor Actions into Exploratory Behavior by Rat. *Curr Biol* **27**, 688-696 (2017).
65. Litwin-Kumar, A., Rosenbaum, R. & Doiron, B. Inhibitory stabilization and visual coding in cortical circuits with multiple interneuron subtypes. *J Neurophysiol* **115**, 1399-409 (2016).
66. Litaudon, P. & Cattarelli, M. Multi-site optical recording of the rat piriform cortex activity. *Neuroreport* **5**, 743-6 (1994).
67. Cazzulino, A.S., Martinez, R., Tomm, N.K. & Denny, C.A. Improved specificity of hippocampal memory trace labeling. *Hippocampus* **26**, 752-62 (2016).
68. Datiche, F., Roullet, F. & Cattarelli, M. Expression of Fos in the piriform cortex after acquisition of olfactory learning: an immunohistochemical study in the rat. *Brain Res Bull* **55**, 95-9 (2001).
69. Roullet, F., Datiche, F., Lienard, F. & Cattarelli, M. Learning-stage dependent Fos expression in the rat brain during acquisition of an olfactory discrimination task. *Behav Brain Res* **157**, 127-37 (2005).

70. Brunjes, P.C. & Osterberg, S.K. Developmental Markers Expressed in Neocortical Layers Are Differentially Exhibited in Olfactory Cortex. *PLoS One* **10**, e0138541 (2015).
71. Diodato, A., Ruinart de Brimont, M., Yim, Y.S., Derian, N., Perrin, S., Pouch, J., Klatzmann, D., Garel, S., Choi, G.B. & Fleischmann, A. Molecular signatures of neural connectivity in the olfactory cortex. *Nat Commun* **7**, 12238 (2016).
72. Beed, P., Gundlfinger, A., Schneiderbauer, S., Song, J., Bohm, C., Burgalossi, A., Brecht, M., Vida, I. & Schmitz, D. Inhibitory gradient along the dorsoventral axis in the medial entorhinal cortex. *Neuron* **79**, 1197-207 (2013).
73. Padmanabhan, K., Osakada, F., Tarabrina, A., Kizer, E., Callaway, E.M., Gage, F.H. & Sejnowski, T.J. Diverse Representations of Olfactory Information in Centrifugal Feedback Projections. *J Neurosci* **36**, 7535-45 (2016).
74. Haberly, L.B. & Price, J.L. Association and commissural fiber systems of the olfactory cortex of the rat. II. Systems originating in the olfactory peduncle. *J Comp Neurol* **181**, 781-807 (1978).
75. Zhao, S., Ting, J.T., Atallah, H.E., Qiu, L., Tan, J., Gloss, B., Augustine, G.J., Deisseroth, K., Luo, M., Graybiel, A.M. & Feng, G. Cell type-specific channelrhodopsin-2 transgenic mice for optogenetic dissection of neural circuitry function. *Nat Methods* **8**, 745-52 (2011).

686

	SST			PV			CB		
Mouse	Slope	R^2	P	Slope	R^2	P	Slope	R^2	P
1	**-0.13 ± 0.03**	**0.48**	**0.0014**	-0.07 ± 0.20	0.02	0.7385	0.08 ± 0.09	0.06	0.3827
2	**-0.22 ± 0.06**	**0.49**	**0.0038**	-0.09 ± 0.16	0.06	0.5977	0.09 ± 0.21	0.01	0.6787
3	-0.04 ± 0.03	0.10	0.2092	-0.38 ± 0.20	0.31	0.0950	**0.67 ± 0.21**	**0.47**	**0.0102**
4	**-0.24 ± 0.03**	**0.85**	**<0.0001**	0.06 ± 0.20	0.01	0.7621	**-0.47 ± 0.07**	**0.79**	**<0.0001**
5	**-0.15 ± 0.03**	**0.61**	**0.001**	**-0.44 ± 0.14**	**0.56**	**0.0124**	**0.44 ± 0.17**	**0.35**	**0.0212**
6	**-0.37 ± 0.05**	**0.86**	**<0.0001**	-0.02 ± 0.14	0.00	0.8698	-0.04 ± 0.10	0.01	0.6900
7	-0.27 ± 0.17	0.25	0.1402						
Fit Average	**-0.25 ± 0.03**	**0.88**	**<0.0001**	**-0.27 ± 0.10**	**0.46**	**0.0305**	0.11 ± 0.17	0.05	0.5538
Slope Dist ≠ 0	**-0.20 ± 0.04**	**-**	**0.0021**	**-0.16 ± 0.08**	**-**	**0.0658**	0.13 ± 0.16	-	0.3700

687

688 **Table 1: Linear regression slope values for fits to normalized density of three classes of**
689 **interneuron versus RC distance in individual mice.** Bold values correspond to significant ($p<0.05$)
690 slope values (mm^{-1}). Linear regression was also performed on the average normalized density across
691 mice versus distance for each interneuron class (Fit Average). P-values correspond to tests for slope
692 not equal to zero. Finally, the distribution of slope values was compared to zero using a non-parametric
693 Mann-Whitney test (distribution ≠ 0). SST- somatostatin interneurons, PV- parvalbumin interneurons,
694 CB- Calbindin interneurons.

695
696
697
698
699
700
701
702
703
704
705
706
707
708

Layer 2	HC			HCO			NEO		
Mouse	Slope	R^2	P	Slope	R^2	P	Slope	R^2	P
1	0.11 ± 0.21	0.03	0.6000	-0.02 ± 0.10	0.01	0.7864	**-0.32 ± 0.13**	**0.29**	**0.0276**
2	-0.14 ± 0.12	0.09	0.2700	-0.40 ± 0.37	0.09	0.3000	0.17 ± 0.26	0.05	0.5100
3	0.60 ± 0.52	0.12	0.2700	-0.17 ± 0.11	0.18	0.1250	-0.18 ± 0.17	0.12	0.3220
4	**1.62 ± 0.38**	**0.61**	**0.0009**	**0.30 ± 0.13**	**0.27**	**0.0370**	-0.08 ± 0.08	0.12	0.3297
5	0.22 ± 0.31	0.04	0.5300	0.10 ± 0.27	0.01	0.7000	**-0.10 ± 0.02**	**0.63**	**0.0032**
6	-0.06 ± 0.13	0.02	0.6400	0.07 ± 0.10	0.04	0.4800	0.0008 ± 0.07	0.00	0.9914
Fit Average	**0.42 ± 0.10**	**0.58**	**0.0016**	-0.06 ± 0.06	0.08	0.2972	-0.09 ± 0.09	0.06	0.3500
Slope Dist ≠ 0	0.39 ± 0.27	-	0.3789	0.01 ± 0.10	-	0.3789	-0.08 ± 0.07	-	0.0658

Layer 3	HC			HCO			NEO		
Mouse	Slope	R^2	P	Slope	R^2	P	Slope	R^2	P
1	**-0.34 ± 0.12**	**0.42**	**0.0224**	**-0.24 ± 0.10**	**0.32**	**0.0330**	**-0.68 ± 0.08**	**0.84**	**<0.0001**
2	-0.16 ± 0.11	0.14	0.17	-0.36 ± 0.33	0.11	0.3100	**-0.37 ± 0.08**	**0.72**	**0.0018**
3	0.37 ± 0.27	0.16	0.2138	-0.22 ± 0.13	0.20	0.1100	**-0.34 ± 0.09**	**0.79**	**0.0060**
4	0.33 ± 0.44	0.04	0.47	-0.11 ± 0.20	0.02	0.5900	**-0.52 ± 0.08**	**0.84**	**0.0002**
5	0.55 ± 0.25	0.33	0.053	-0.03 ± 0.14	0.00	0.8000	**-0.39 ± 0.09**	**0.66**	**0.0023**
6	0.02 ± 0.27	0.00	0.9427	**-0.29 ± 0.10**	**0.37**	**0.0120**	**-0.39 ± 0.08**	**0.64**	**0.0003**
Fit Average	0.20 ± 0.11	0.21	0.11	**-0.19 ± 0.04**	**0.58**	**0.0005**	**-0.47 ± 0.04**	**0.94**	**<0.0001**
Slope Dist ≠ 0	0.13 ± 0.14	-	0.3789	**-0.21 ± 0.05**	-	**0.0050**	**-0.45 ± 0.05**	-	**0.0050**

Table 2: Linear regression slope values for fits to normalized density of tdTom(+) cells versus RC distance in individual mice. Bold values correspond to significant ($p<0.05$) slope values (mm^{-1}). Underlined values correspond to the cohort of mice exposed to ethyl butyrate (HCO, NEO only) and the remaining mice were exposed isoamyl acetate. Linear regression was also performed on the average normalized density across mice versus distance (Fit Average). P-values correspond to tests for slope not equal to zero. Finally, the distribution of slope values was compared to zero using a non-parametric Mann-Whitney test (distribution ≠ 0). HC- home cage, HCO- home cage plus odor, NEO- novel environment plus odor.

722 **Figure Legends**

723 **Figure 1: Caudally biased, asymmetric inhibition of pyramidal cells in APC. A)** Schematic of grid-
724 stimulation paradigm for L2 excitatory neurons- semilunar cells (SL) and superficial (s) pyramidal cells
725 (sPCs). VG- interneuron expressing ChR2 under VGAT promoter. R: rostral, C: caudal. **B1)** IPSCs
726 recorded during focal light stimulation at each grid location in a representative SL cell. Scale bars:
727 vertical 100 pA, horizontal 200 ms. Red trace indicates location of recorded cell. **B2)** Bias values are
728 uniformly distributed across SL cells. Negative values correspond to greater average inhibition from
729 rostral sites and positive values correspond to greater inhibition from caudal sites. **C1)** IPSCs recorded
730 from a representative L2 sPC. **C2)** Predominantly positive bias values in sPCs indicates stronger
731 inhibition from caudal versus rostral sites (* $p<0.05$, n=14, one sample t-test). Scale bars: vertical 100
732 pA, horizontal 200 ms. **D1)** Schematic of grid-stimulation paradigm for L3 deep pyramidal cells (dPCs).
733 **D2)** IPSCs recorded from a representative L3 dPC. Scale bars: vertical 200 pA, horizontal 200 ms. **D3)**
734 Predominantly positive bias values in dPCs indicates stronger inhibition from caudal versus rostral sites
735 (** $p<0.01$, n=16, one sample t-test). **E1)** Recordings of two dPCs in the same slice indicate that the
736 caudal (C) neuron of a pair receives stronger inhibition than the rostral (R) neuron (**$p<0.01$, n=19
737 pairs, paired t-test). IPSCs were evoked using a 70 μm light spot centered on the soma of the recorded
738 PC. **E2)** The difference in inhibition (pAs) between the caudal (C) and rostral (R) cell in each pair (E1)
739 is plotted against the difference in RC distance between the two cells. As the distance between the two
740 cells increases, the difference in inhibition also increases (* $p<0.05$, linear regression, n=19). **F)**
741 Inhibitory strength versus RC position of the dPC relative to the rostral start of the LOT in the sagittal
742 slice. Inhibition increases with RC distance (**$p<0.01$, linear regression, n=27).

743 **Figure 2: Rostrally biased, asymmetric inhibition of L3 interneurons. A)** Schematic of grid-
744 stimulation paradigm for L2 and L3 inhibitory neurons (INT). **B)** Inhibition is significantly stronger in L3
745 INT (filled green circles) than L2 INT (** $p<0.01$, ANOVA, open green circles) but did not significantly
746 differ from L3 dPCs (solid black triangles). Values correspond to the maximum IPSC for each cell
747 regardless of location in grid. **C1)** IPSCs recorded during focal light stimulation at each grid location in

748 a representative L2 INT. Scale bars: vertical 100 pA, horizontal 200 ms. Red trace indicates location of
749 recorded cell. **C2)** The bias values for L2 INTs do not differ from zero. **D1)** IPSCs recorded from a
750 representative L3 INT. Scale bars: vertical 200 pA, horizontal 200 ms. **D2)** Asymmetric distribution of
751 bias values in dPCs indicates stronger inhibition from rostral versus caudal sites (** $p<0.05$, n=25, one
752 sample t-test). **E)** The bias values of dPCs (black triangles) significantly differed from L3 INTs (**
753 $p<0.01$, unpaired t-test, green circles). **F)** Average inhibitory strength across rostral (I_R) or caudal (I_C)
754 sites in dPCs (black triangles) and L3 INT (green circles). Opposing inhibitory asymmetries: in dPCs,
755 average I_C was significantly greater than I_R (black ** $p<0.01$ paired t-test), while I_R was significantly
756 greater than I_C I in L3 INTs (green ** $p<0.01$, paired t-test).

757 **Figure 3: Rostral-caudal distributions of L3 interneurons. A1)** Representative coronal sections from
758 rostral (0-200 µm, left) and caudal (within last 300 µm, right) APC showing SST-tdTom(+) cells in L3
759 region of interest (ROI, dashed line). Scale bar: 500 µm **A2)** Normalized density versus RC distance for
760 the mouse shown in A1 (SST-mouse #2, **Table 1**, ** $p<0.01$. **A3)** Normalized density of SST-cells
761 versus distance for all mice (open circles). The average (± SE, n=7) normalized density of SST cells
762 across mice significantly decreased with RC distance (red circles, **$p<0.01$). **A4)** Distribution of slopes
763 from linear fits to data from individual mice. Solid circles indicate significantly negative slopes ($p<0.05$).
764 The distribution of slope values was significantly non-zero (** p: 0.002 MWU-test). **B1-4)** As in A1-4,
765 except for Calbindin(+) interneurons (CB). **B1,2)** Data from CB mouse #5 in **Table 1**. **B3**) On average,
766 there is no change in density of CB cells along the RC axis (filled green circles, p: 0.55). **B4)** In
767 individual mice CB cells significantly increased or decreased (filled green circles) along the RC axis, but
768 the distribution of slopes did not differ from zero (p: 0.37, MWU-test). **C1-4)** As in A1-4, except for
769 Parvalbumin(+) interneurons (PV). **B1,2)** Data from PV mouse #6 in **Table 1**. **C3**) On average, the
770 density of PV cells decreased along the RC axis (filled black circles, p: 0.03). **C4)** However, only one
771 mouse showed a significant decrease in PV cells along the RC axis (filled black circle) and the
772 distribution of slopes did not differ from zero (p: 0.07, MWU-test).

773 **Figure 4: Spatial profiles of SST-cell mediated inhibition of L3 pyramidal cells and interneurons.**
774 **A)** Schematic of grid-stimulation paradigm for L3 dPCs and inhibitory neurons (INT) in sagittal sections
775 from SST-ChR2 mice. **B1)** IPSCs recorded during focal light stimulation at each grid location in a
776 representative L3 INT. Scale bars: vertical 200 pA, horizontal 200 ms. Red trace indicates location of
777 recorded cell. **B2)** The distribution of bias values for L3 INTs is significantly rostrally biased (*$p<0.05$,
778 one sample t-test, blue line) and does not differ from VGAT-ChR2 animals (green line). **C1)** IPSCs
779 recorded from a representative L3 dPC. Scale bars: vertical 100 pA, horizontal 200 ms. **C2)** The
780 distribution of bias values in dPCs is not asymmetric with a mean near zero (blue line) compared to a
781 caudally biased mean in VGAT-ChR2 animals (green line). **D)** Normalized inhibition on rostral versus
782 caudal sides in VGAT-ChR2 (green) and SST-ChR2 (blue) mice is significantly asymmetric and
783 rostrally biased in L3 interneurons (circles, Left). SST-ChR2 mediated inhibition is not significantly
784 asymmetric in dPCs (right triangles, SST-ChR2: blue, VGAT-ChR2: green). **E)** Schematic of
785 optogenetic stimulation of VGAT-ChR2(+) interneurons (green) including SST-cells which also express
786 the inhibitory DREADD, (SST-Di, black with green outline). **F)** IPSCs in response to optogenetic
787 activation of L3 rostral and caudal sites in control (green) and CNO (black). **G)** Change in RC bias
788 ($Bias_{CNO}$-$Bias_{Pre}$) in the presence of CNO. Inhibition became less caudally biased in n=8 cells (negative
789 values, black bars) in CNO but more caudally biased in n=4 cells (positive values, gray bars).

790 **Figure 5: Spatial profiles of neural activity in APC following odor exposure. A)** tdTom(+) cells
791 from a Fos^{ERT}xAi14 mouse in rostral (left) and caudal (right) sections from (NEO condition). Dashed
792 lines delineate Layers 2 and 3 and the lateral olfactory tract (lot). DAPI stain for nuclei (blue). **B1, B2)**
793 Schematics of experimental schedule (**B1**) and contexts **(B2)**. Abbreviations: HC: home cage, HCO:
794 home cage plus odor, NEO: Novel environment plus odor, 4-OHT: 4-hydroxytamoxifen. **B3**) Location of
795 an example mouse in the NEO arena during 30 min odor exposure. Mice continuously move between
796 the odorized (orange circle (+)) and non-odor arms (blank circle (-)) as well as the center (C) of the
797 arena. **C, D)** Normalized density of tdTom(+) cells along the RC axis of L2 **(C)** and L3 (**D).** Open
798 triangles: data from individual animals; filled triangles: average across animals. **E)** Slopes of linear fits

799 to density versus distance for individual mice in each condition in L2 (**E1**) and L3 (**E2**). Filled triangles
800 indicate slopes significantly different from zero ($p<0.05$, see **Table 1** for p: values). **E2**) In L3, the
801 distribution of slopes in HCO and NEO animals significantly differed from 0 (** $p<0.01$, MWU-test).
802 Further the distribution of slopes in NEO animals significantly differed from HC and HCO animals (★★
803 $p<0.01$, KW-test). **F)** The average density of neurons increases with odor exposure (HCO, NEO) in L2
804 (**F1, *** $p<0.05$, KW-test) but not L3 **(F2)**.

805 **Figure 6: The spatial profiles of inhibition are commensurate with neural activity along the RC**
806 **axis of APC. A1)** Schematic summarizing rostral-caudal spatial profiles of inhibition (green), SST-
807 interneuron density and SST-mediated inhibition of interneurons (blue) and active neurons in L3 of
808 NEO mice (red). **A2)** Proposed disinhibitory circuit consisting of a higher density of rostral SST-cells
809 (blue) that inhibit interneurons (light green) and disinhibit PCs increasing rostral neural activity (red
810 PCs). In caudal APC, lower density of SST-cells allows greater inhibition (dark green) and less active
811 PCs (black). **B)** Normalized density of active neurons (red triangles) decreases along the RC axis
812 (slope: -0.47 mm^{-1}, R^2:0.94, $p<0.0001$, from **Figure 5D3**), as normalized inhibition of dPCs increases
813 (slope: +0.67 mm^{-1}, R^2:0.95, $p<0.0001$, from **Figure 1F**). Because there are only two points at 1.5 mm
814 in **Figure 1F**, inhibitory strength was normalized to a projected "maximum" strength (8.17 pAs) at 1.6
815 mm, based on the linear fit to inhibitory strength versus distance.

816

817

818

819

820

821

822

823

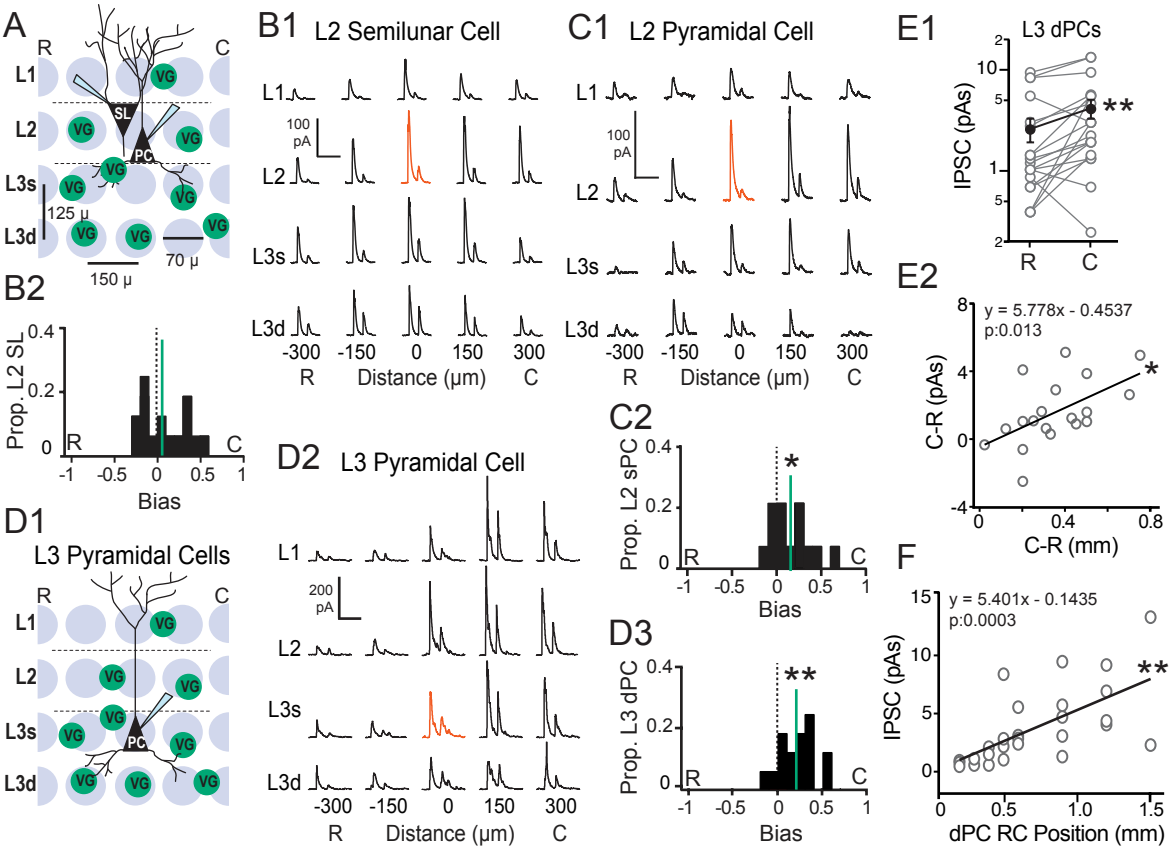

Figure 1: Caudally biased, asymmetric inhibition of pyramidal cells in APC. A) Schematic of grid-stimulation paradigm for L2 excitatory neurons- semilunar cells (SL) and superficial (s) pyramidal cells (sPCs). VG- interneuron expressing ChR2 under VGAT promoter. R: rostral, C: caudal. B1) IPSCs recorded during focal light stimulation at each grid location in a representative SL cell. Scale bars: vertical 100 pA, horizontal 200 ms. Red trace indicates location of recorded cell. B2) Bias values are uniformly distributed across SL cells. Negative values correspond to greater average inhibition from rostral sites and positive values correspond to greater inhibition from caudal sites. C1) IPSCs recorded from a representative L2 sPC. C2) Predominantly positive bias values in sPCs indicates stronger inhibition from caudal versus rostral sites (* $p<0.05$, n=14, one sample t-test). Scale bars: vertical 100 pA, horizontal 200 ms. D1) Schematic of grid-stimulation paradigm for L3 deep pyramidal cells (dPCs). D2) IPSCs recorded from a representative L3 dPC. Scale bars: vertical 200 pA, horizontal 200 ms. D3) Predominantly positive bias values in dPCs indicates stronger inhibition from caudal versus rostral sites (** $p<0.01$, n=16, one sample t-test). E1) Recordings of two dPCs in the same slice indicate that the caudal (C) neuron of a pair receives stronger inhibition than the rostral (R) neuron (**$p<0.01$, n=19 pairs, paired t-test). IPSCs were evoked using a 70 µm light spot centered on the soma of the recorded PC. E2) The difference in inhibition (pAs) between the caudal (C) and rostral (R) cell in each pair (E1) is plotted against the difference in RC distance between the two cells. As the distance between the two cells increases, the difference in inhibition also increases (* $p<0.05$, linear regression, n=19). F) Inhibitory strength versus RC position of the dPC relative to the rostral start of the LOT in the sagittal slice. Inhibition increases with RC distance (**$p<0.01$, linear regression, n=27).

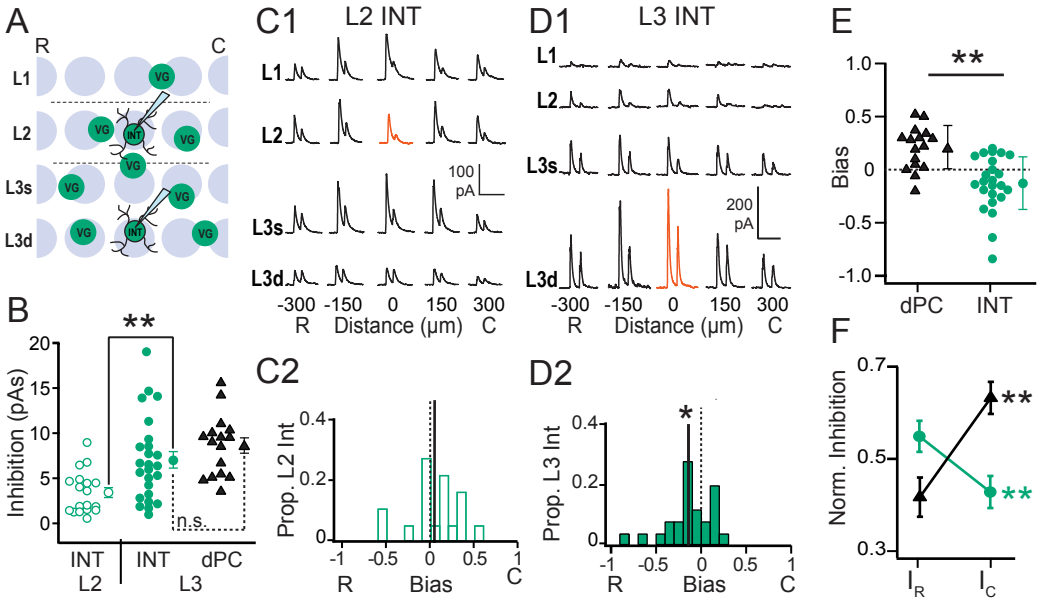

Figure 2: Rostrally biased, asymmetric inhibition of L3 interneurons. A) Schematic of grid-stimulation paradigm for L2 and L3 inhibitory neurons (INT). B) Inhibition is significantly stronger in L3 INT (filled green circles) than L2 INT (** p<0.01, ANOVA, open green circles) but did not significantly differ from L3 dPCs (solid black triangles). Values correspond to the maximum IPSC for each cell regardless of location in grid. C1) IPSCs recorded during focal light stimulation at each grid location in a representative L2 INT. Scale bars: vertical 100 pA, horizontal 200 ms. Red trace indicates location of recorded cell. C2) The bias values for L2 INTs do not differ from zero. D1) IPSCs recorded from a representative L3 INT. Scale bars: vertical 200 pA, horizontal 200 ms. D2) Asymmetric distribution of bias values in dPCs indicates stronger inhibition from rostral versus caudal sites (** p<0.05, n=25, one sample t-test). E) The bias values of dPCs (black triangles) significantly differed from L3 INTs (** p<0.01, unpaired t-test, green circles). F) Average inhibitory strength across rostral (IR) or caudal (IC) sites in dPCs (black triangles) and L3 INT (green circles). Opposing inhibitory asymmetries: in dPCs, average IC was significantly greater than IR (black ** p<0.01 paired t-test), while IR was significantly greater than IC I in L3 INTs (green ** p<0.01, paired t-test).

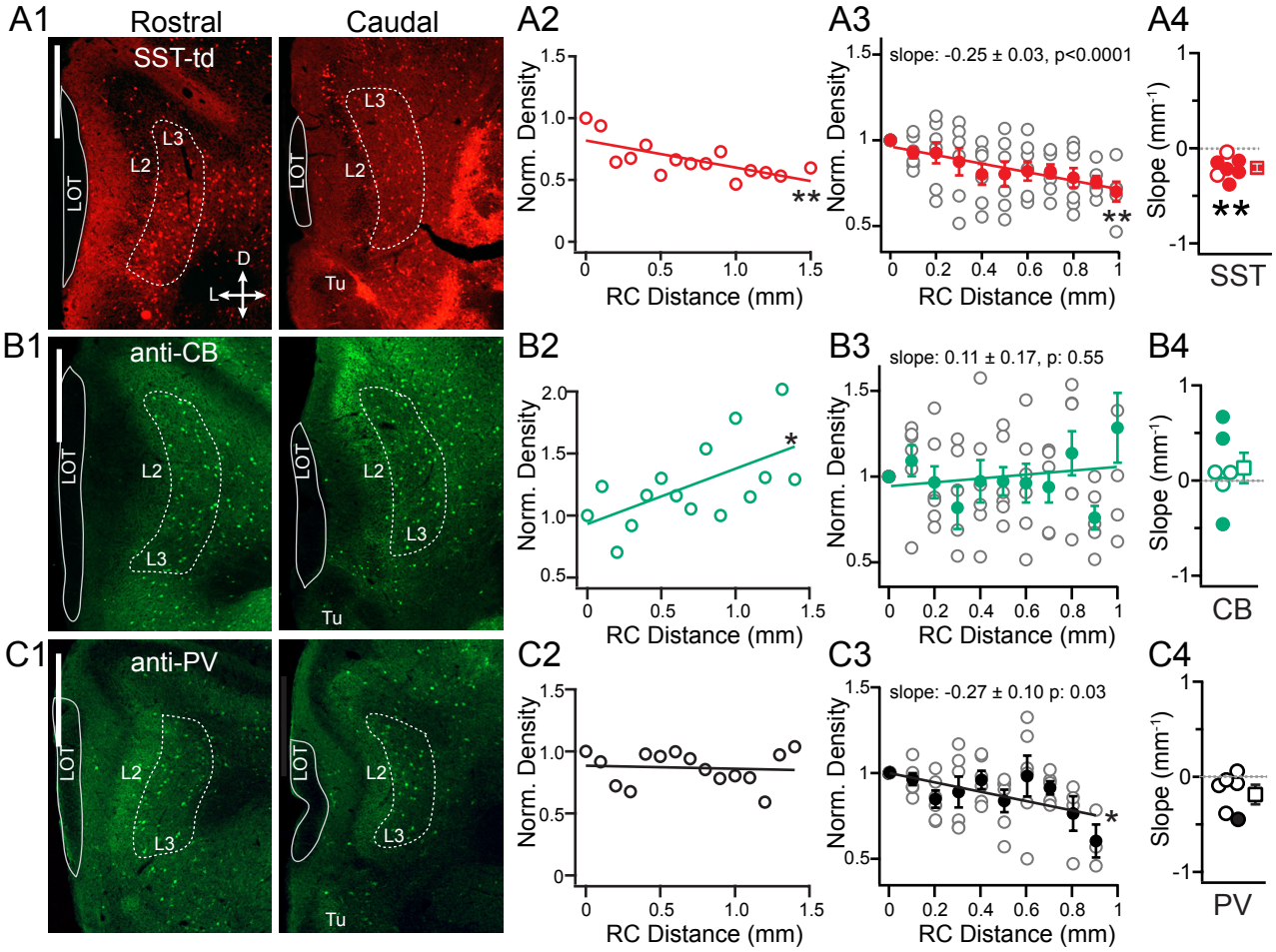

Figure 3: Rostral-caudal distributions of L3 interneurons. A1) Representative coronal sections from rostral (0-200 µm, left) and caudal (within last 300 µm, right) APC showing SST-tdTom(+) cells in L3 region of interest (ROI, dashed line). Scale bar: 500 µm A2) Normalized density versus RC distance for the mouse shown in A1 (SST-mouse #2, Table 1, ** p<0.01. A3) Normalized density of SST-cells versus distance for all mice (open circles). The average (± SE, n=7) normalized density of SST cells across mice significantly decreased with RC distance (red circles, **p<0.01). A4) Distribution of slopes from linear fits to data from individual mice. Solid circles indicate significantly negative slopes (p<0.05). The distribution of slope values was significantly non-zero (** p: 0.002 MWU-test). B1-4) As in A1-4, except for Calbindin(+) interneurons (CB). B1,2) Data from CB mouse #5 in Table 1. B3) On average, there is no change in density of CB cells along the RC axis (filled green circles, p: 0.55). B4) In individual mice CB cells significantly increased or decreased (filled green circles) along the RC axis, but the distribution of slopes did not differ from zero (p: 0.37, MWU). C1-4) As in A1-4, except for Parvalbumin(+) interneurons (PV). B1,2) Data from PV mouse #6 in Table 1. C3) On average, the density of PV cells decreased along the RC axis (filled black circles, p: 0.03). C4) However, only one mouse showed a significant decrease in PV cells along the RC axis (filled black circle) and the distribution of slopes did not differ from zero (p: 0.07, MWU).

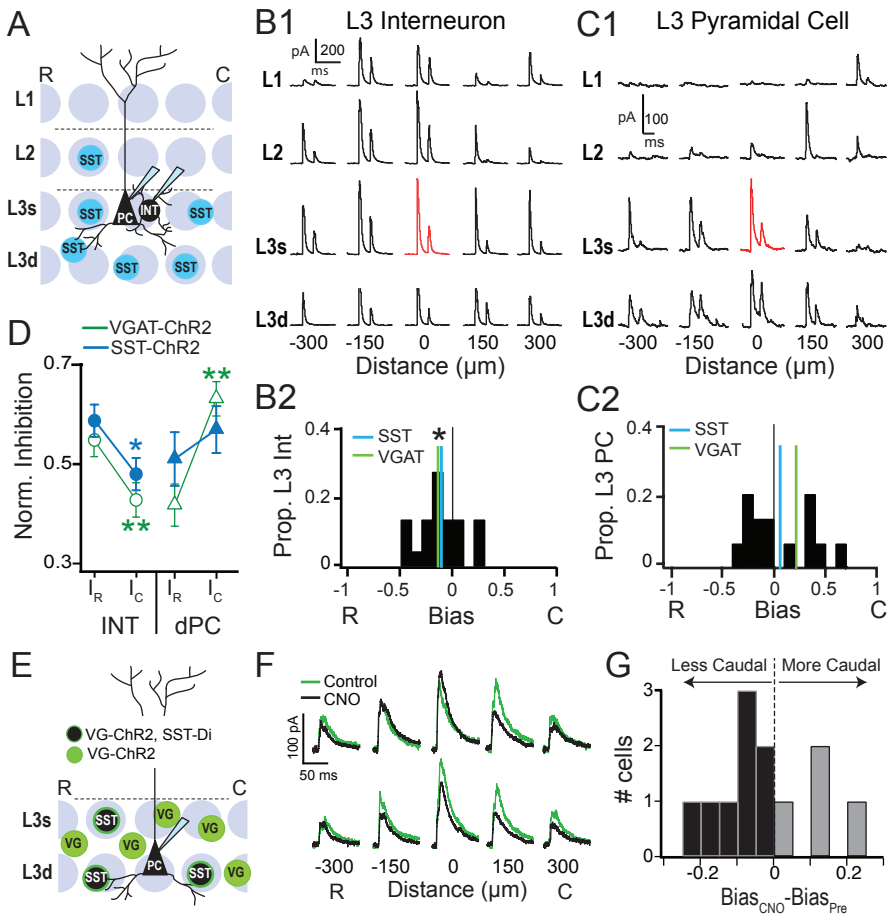

Figure 4: Spatial profiles of SST-cell mediated inhibition of L3 pyramidal cells and interneurons. A) Schematic of grid-stimulation paradigm for L3 dPCs and inhibitory neurons (INT) in sagittal sections from SST-ChR2 mice. B1) IPSCs recorded during focal light stimulation at each grid location in a representative L3 INT. Scale bars: vertical 200 pA, horizontal 200 ms. Red trace indicates location of recorded cell. B2) The distribution of bias values for L3 INTs is significantly rostrally biased (*p<0.05, one sample t-test, blue line) and does not differ from VGAT-ChR2 animals (green line). C1) IPSCs recorded from a representative L3 dPC. Scale bars: vertical 100 pA, horizontal 200 ms. C2) The distribution of bias values in dPCs is not asymmetric with a mean near zero (blue line) compared to a caudally biased mean in VGAT-ChR2 animals (green line). D) Normalized inhibition on rostral versus caudal sides in VGAT-ChR2 (green) and SST-ChR2 (blue) mice is significantly asymmetric and rostrally biased in L3 interneurons (circles, Left). SST-ChR2 mediated inhibition is not significantly asymmetric in dPCs (right triangles, SST-ChR2: blue, VGAT-ChR2: green). E) Schematic of optogenetic stimulation of VGAT-ChR2(+) interneurons (green) including SST-cells which also express the inhibitory DREADD, (SST-Di, black with green outline). F) IPSCs in response to optogenetic activation of L3 rostral and caudal sites in control (green) and CNO (black). G) Change in RC bias (BiasCNO-BiasPre) in the presence of CNO. Inhibition became less caudally biased in n=8 cells (negative values, black bars) in CNO but more caudally biased in n=4 cells (positive values, gray bars).

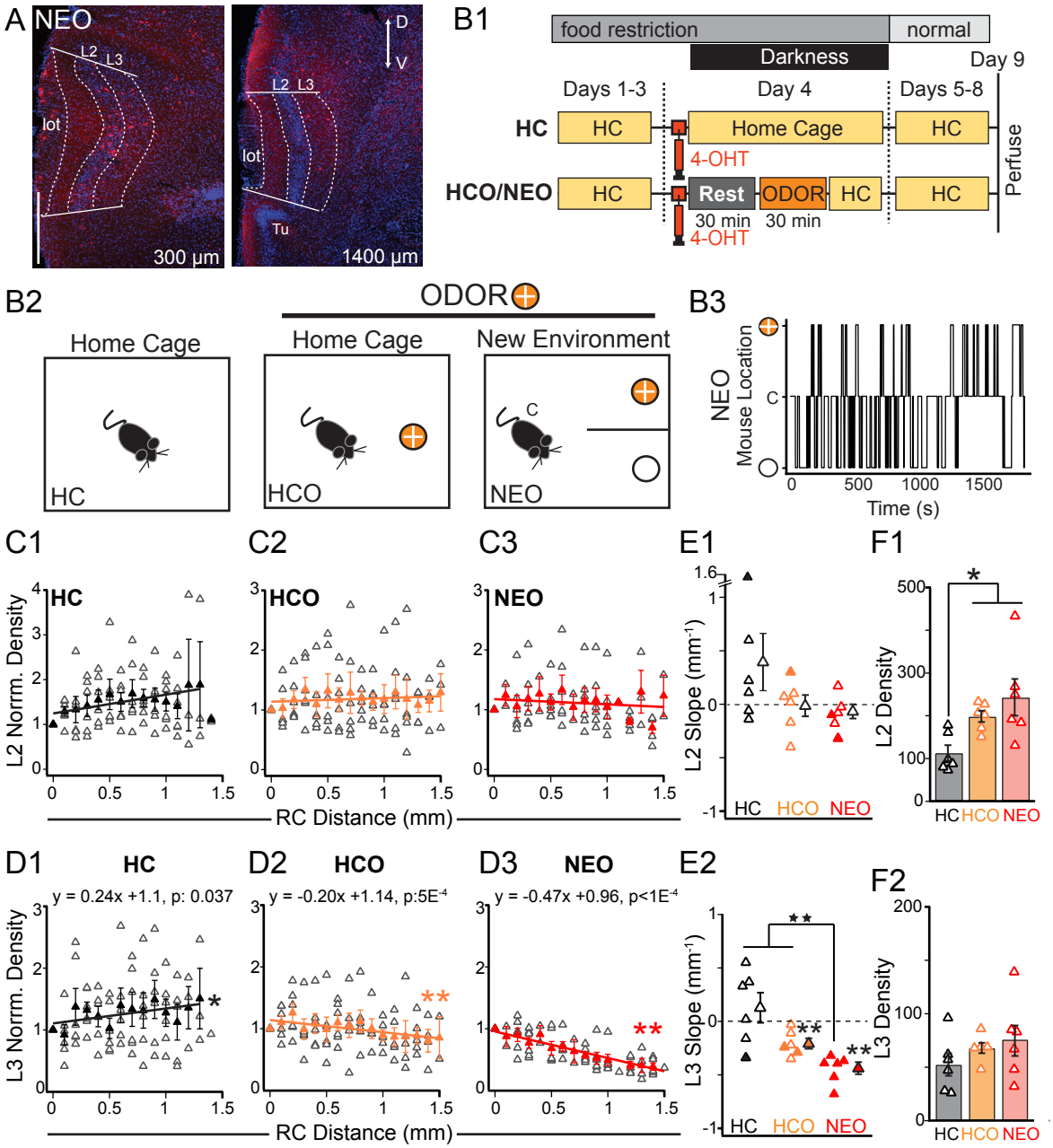

Figure 5: Spatial profiles of neural activity in APC following odor exposure. A) tdTom(+) cells from a FosERTxAi14 mouse in rostral (left) and caudal (right) sections from (NEO condition). Dashed lines delineate Layers 2 and 3 and the lateral olfactory tract (lot). DAPI stain for nuclei (blue). B1, B2) Schematics of experimental schedule (B1) and contexts (B2). Abbreviations: HC: home cage, HCO: home cage plus odor, NEO: Novel environment plus odor, 4-OHT: 4-hydroxytamoxifen. B3) Location of an example mouse in the NEO arena during 30 min odor exposure. Mice continuously move between the odorized (orange circle (+)) and non-odor arms (blank circle (-)) as well as the center (C) of the arena. C, D) Normalized density of tdTom(+) cells along the RC axis of L2 (C) and L3 (D). Open triangles: data from individual animals; filled triangles: average across animals. E) Slopes of linear fits to density versus distance for individual mice in each condition in L2 (E1) and L3 (E2). Filled triangles indicate slopes significantly different from zero ($p<0.05$, see Table 1 for p: values). E2) In L3, the distribution of slopes in HCO and NEO animals significantly differed from 0 (** $p<0.01$, MWU-test). Further the distribution of slopes in NEO animals significantly differed from HC and HCO animals (⋆⋆ $p<0.01$, KW-test). F) The average density of neurons increases with odor exposure (HCO, NEO) in L2 (F1, * $p<0.05$, KW-test) but not L3 (F2).

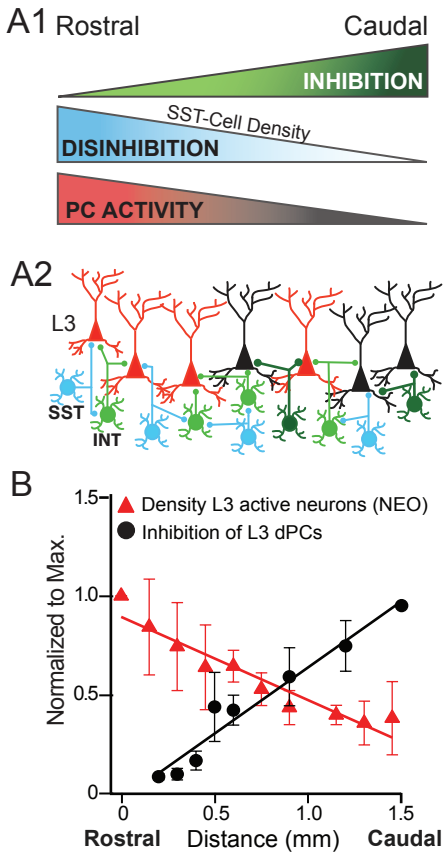

Figure 6: The spatial profiles of inhibition are commensurate with neural activity along the RC axis of APC. A1) Schematic summarizing rostral-caudal spatial profiles of inhibition (green), SST-interneuron density and SST-mediated inhibition of interneurons (blue) and active neurons in L3 of NEO mice (red). A2) Proposed disinhibitory circuit consisting of a higher density of rostral SST-cells (blue) that inhibit interneurons (light green) and disinhibit PCs increasing rostral neural activity (red PCs). In caudal APC, lower density of SST-cells allows greater inhibition (dark green) and less active PCs (black). B) Normalized density of active neurons (red triangles) decreases along the RC axis (slope: -0.47 mm-1, R^2: 0.94, $p<0.0001$, from Figure 5D3), as normalized inhibition of dPCs increases (slope: +0.67 mm-1, R^2: 0.95, $p<0.0001$, from Figure 1F). Because there are only two points at 1.5 mm in Figure 1F, inhibitory strength was normalized to a projected "maximum" strength (8.17 pAs) at 1.6 mm, based on the linear fit to inhibitory strength versus

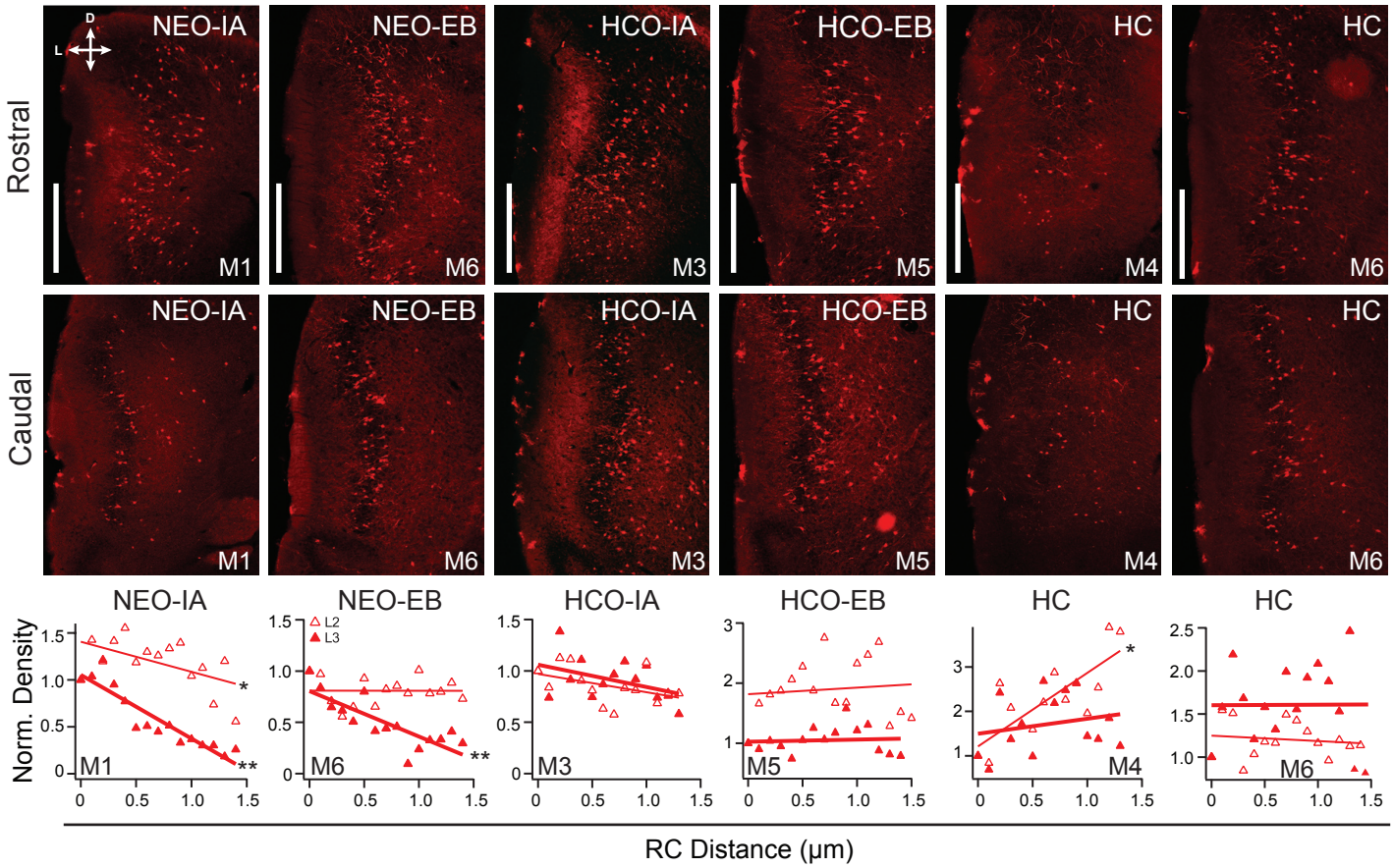

Supplemental Figure 1: Fos-tdTom(+) cells in anterior piriform cortex (APC) . Representative coronal sections from the rostral (0-200 μm, upper row) and caudal (within last 300 μm, middle row) APC showing fos-tdTom(+) cells activated during novel odor exposure in a novel environment (NEO) or the home cage (HCO), or the home cage with no odor (HC). Bottom row: Normalized density (Layer 2, open triangles, L3 filled triangles) versus distance along the RC axis of Fos-tdTom(+) cells for the mouse corresponding to the sections above. Linear regression fits (thin lines, L2: thick lines, L3) with slopes that significantly differed from zero are indicated by astrisks: * $p<0.05$, or ** $p<0.01$. Each column is data from an individual mouse and the mouse number (M1-6) matches the mouse numbers in Table 2 (main text). Responses to isoamyl-acetate (IA, left) or ethyl butyrate (EB, right) are shown for each odor condition.

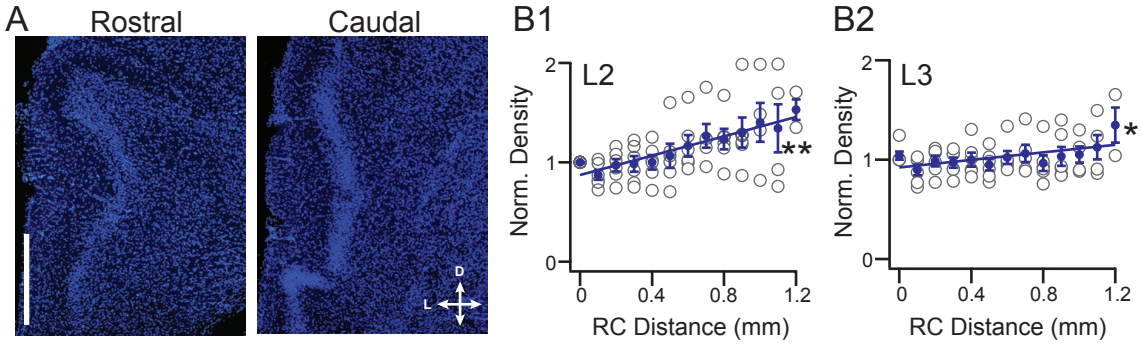

C

	L2			L3		
Condition	Slope	R^2	P	Slope	R^2	P
NEO	**0.78 ± 0.12**	**0.74**	**<0.0001**	**0.35 ± 0.09**	**0.55**	**0.0014**
NEO	**1.48 ± 0.11**	**0.91**	**<0.0001**	**0.43 ± 0.12**	**0.56**	**0.0046**
HCO	0.10 ± 0.14	0.039	0.5145	-0.08 ± 0.07	0.10	0.2919
HCO	0.05 ± 0.13	0.0171	0.7184	**-0.24 ± 0.08**	**0.53**	**0.0169**
HC	**0.30± 0.5**	**0.8059**	**0.0002**	-0.09 ± 0.06	0.19	0.1753
HC	**0.52 ± 0.14**	**0.86**	**<0.0001**	0.07 ± 0.08	0.09	0.3805
Fit Avg	**0.48 ± 0.05**	**0.91**	**<0.0001**	**0.10 ± 0.4**	**0.36**	**0.0390**
Slope ≠ 0	**0.54 ± 0.21**	**-**	**0.0051**	0.08 ± 0.1	-	0.9360

Supplemental Figure 2: DAPI staining in anterior piriform cortex (APC) . Representative coronal sections from rostral (0-200 µm, upper row) and caudal (within last 300 µm) APC showing DAPI(+) nuclei from mice exposed to novel odor exposure in a novel environment (NEO). B) Bottom row: Normalized density versus distance along the RC axis of DAPI(+) cells for individual mice (open circles) and average across mice (blue filled circles) in L2 (B1) and L3 (B2). Linear regression fits of average data have slopes that significantly differed from zero are indicated by astrisks: * $p<0.05$, or ** $p<0.01$. C) Table with slope (mm^{-1}) data and statistics for each animal. Bold numbers correspond to significant slopes ($p<0.05$). Fit average corresponds to the linear fits shown in (B). The slope distribution was significantly different from zero for L2 but not L3. HCO: home cage + odor, or the home cage with no odor (HC). Scale: 500 µm

Location		Distribution ≠ 0	Mean S1	SE	SD	Test	P	n	α: 0.05 1-β
Figure 1		bias SL ≠ 0	0.08	0.11	0.39661064	1 sample t-test	0.49	13	0.12
		bias sPC ≠ 0	0.22	0.08	0.299332591	1 sample t-test	**0.016**	14	0.85
		bias dPC ≠ 0	0.19	0.05	0.2	1 sample t-test	**0.0012**	16	0.9673
Figure 2		bias L2 INT ≠ 0	0.04	0.07	0.296984848	1 sample t-test	0.11	18	0.09
		bias L3 INT ≠ 0	-0.13	0.05	0.25	1 sample t-test	**0.013**	25	0.74
Figure 4		bias L3 INT ≠ 0 SST	0.11	0.04	0.18761663	1 sample t-test	**0.02**	22	0.81
		bias dPC ≠ 0 SST	0.06	0.08	0.299332591	1 sample t-test	0.45	14	
		bias dPC ≠ 0 CNO	0.17	0.08	0.277128129	1 sample t-test	0.051	12	0.74
		bias dPC ≠ 0 PRE	0.19	0.06	0.207846097	1 sample t-test	**0.01**	12	0.91
Figure 3	TABLE 1 dist ≠ 0	Slope SST ≠ 0	-0.2	0.04	0.105830052	MWU-test	**0.0021**	7	0.99
		Slope PV ≠ 0	-0.16	0.08	0.195959179	MWU-test	0.0658	6	0.54
		Slope CB ≠ 0	0.13	0.16	0.391918359	MWU-test	0.37	6	0.12
Figure 5	TABLE 2 dist ≠ 0	Slope HC L2 ≠ 0	0.39	0.27	0.661362231	MWU-test	0.3789	6	0.3
		Slope HC L3 ≠ 0	0.13	0.14	0.342928564	MWU-test	0.3789	6	0.16
		Slope HCO L2 ≠ 0	0.01	0.1	0.244948974	MWU-test		6	0.05
		Slope HCO L3 ≠ 0	-0.21	0.05	0.122474487	MWU-test	**0.005**	6	0.99
		Slope NEO L2 ≠ 0	-0.08	0.07	0.171464282	MWU-test	0.065	6	0.21
		Slope NEO L3 ≠ 0	-0.45	0.05	0.122474487	MWU-test	**0.005**	6	1

Supplemental Table 1: Summary stats for one sample t-test and Mann-Whitney U-test (MWU). M-mean, SD-standard deviation, SE- standard error, n- number of samples, "1-β" power analysis results at α: 0.05 given sample number**.** Bold: Significant p-values, red : 1-β < 0.7.

Location		Regression	slope	R^2	R	Test	P	n	α: 0.05 1-β
Figure 1		Diff IPSC vs Diff Dist	5.8	0.32	0.565685425	F-test	**0.013**	19	0.7
		IPSC vs RC Dist	5.4	0.41	0.640312424	F-test	**0.003**	27	1
Figure 3	Table 1	SST-M1	-0.13	0.48	0.692820323	F-test	**0.0014**	18	0.9
		SST -M6	-0.38	0.86	0.92736185	F-test	**1.00E-05**	12	0.9
		SST -AVG	-0.25	0.88	0.938083152	F-test	**1.00E-05**	10	0.9
		PV-M5	-0.44	0.56	0.748331477	F-test	**0.012**	10	0.75
		PV-Avg	-0.27	0.46	0.678232998	F-test	**0.03**	10	0.6
		CB-M3	0.67	0.46	0.678232998	F-test	**0.01**	13	0.75
		CB-M5	0.44	0.35	0.591607978	F-test	**0.021**	15	0.67
Figure 5	Table 2	HC L2-M4	1.62	0.61	0.781024968	F-test	**0.0009**	14	0.9
		HC-L2 Avg	0.42	0.577	0.759605161	F-test	**0.016**	13	0.85
		HC L3	-0.34	0.42	0.64807407	F-test	**0.022**	12	0.65
		HCO-L2- M4	0.3	0.27	0.519615242	F-test	**0.037**	16	0.55
		HCO-L3-M1	-0.24	0.32	0.565685425	F-test	**0.033**	14	0.55
		HCO-L3-M6	-0.29	0.37	0.608276253	F-test	**0.012**	16	0.7
		HCO-L3-Avg	-0.19	0.58	0.761577311	F-test	**0.0005**	16	0.9
		NEO-L2-M1	-0.32	0.29	0.538516481	F-test	**0.0276**	15	0.55
		NEO-L2-M5	-0.1	0.63	0.793725393	F-test	**0.0032**	11	0.85
		NEO-L3-M3	-0.34	0.63	0.793725393	F-test	**0.006**	10	0.8
Figure 5, 6, Table 2		NEO-L3-Avg	-0.47	0.94	0.969535971	F-test	**0.0001**	14	0.95
Figure 6		IPSC vs RC Dist	0.67	0.95	0.974679434	F-test	**0.0001**	27	1

Supplemental Table 2: Summary stats for F-test for non-zero slope of linear regression. n- number of samples, "1-β" power analysis results at α: 0.05 given sample number**.** Bold: Significant p-values, red : 1-β < 0.7. For density measures, power was analyzed for the mice yielding significant results but the lowest R-values and the lowest number of samples. These represent the minimum power for significant findings within the group.

Location	Comparison	M1	SD1	N1	M2	SD2	N2	M diff	SD diff	Test	F	P	α: 0.05 1-β
Figure 1	IPSC strength C vs R dPCs	4.18	3.92	19	2.6	2.96	19	1.58	1.94	paired t-test		**0.002**	0.8
	IPSC strength L2 vs L3 INT	3.42	2.12	18	7.02	4.60	25			ANOVA-Tukey	0.44	**0.0043**	0.8
Figure 2	IPSC strength L3 dPC vs INT	7.02	4.60	25	8.63	3.66	19			ANOVA-Tukey	0.19	n.s.	0.22
	IPSC strength C vs R INT	0.54	0.17	25	0.43	0.17	25	0.12	0.2	paired t-test		**0.008**	0.8
	IPSC strength C vs R PC	0.63	0.14	16	0.44	0.17	16	0.19	0.21	paired t-test		**0.003**	0.8
Figure 3	Density PV < SST cells	109	22.05	6	235	37.04	7			Kruskal-Wallis		**0.0054**	0.8
	Density PV < CB cells	109	22.05	6	174	66.14	6			Kruskal-Wallis		**0.0054**	0.4
Figure 4	IPSC strength C vs R INT SST	0.58	0.14	22	0.479	0.15	22	0.11	0.19	paired t-test		**0.017**	0.75
	IPSC strength VGAT vs SST INT	6.82	6.57	22	7.02	4.60	25			unpaired t-test		0.91	0.05
	IPSC strength C vs PC SST	0.51	0.12	15	0.57	0.12	15	0.06	0.32	paired t-test		0.5	0.05
	IPSC strength VGAT vs SST PC	4.77	3.21	13	8.63	3.66	19			unpaired t-test		**0.003**	0.91
	IPSC strength Pre vs CNO	4.14	2.42	12	2.72	1.39	12	1.42	1.53	paired t-test		**0.007**	0.8
	IPSC strength C vs R PC CNO	35	25.46	8	24	19.80	8	9	7	Wilcoxon Signed Rank		**<0.05**	0.8
Figure 5	Density HC vs HCO L2	113	44.09	6	199	31.84	6			Kruskal-Wallis		**0.013**	0.9
	Density HC vs NEO L2	113	44.09	6	243	105.3	6			Kruskal-Wallis		**0.013**	0.6
	Density HC vs HCO L3	52	26.94	6	68	12.25	6			Kruskal-Wallis		0.149	0.19
	Density HC vs NEO L3	52	26.94	6	76	36.74	6			Kruskal-Wallis		0.149	0.21

Supplemental Table 3: Summary stats for two sample comparisons. M-mean, SD-standard deviation, n- number of samples, "1-β" power analysis results at α: 0.05 given sample number**.** Bold: Significant p-values, red : 1-β < 0.7.